ALMA MATER STUDIORUM · UNIVERSITÀ DI BOLOGNA

Scuola di Scienze
Dipartimento di Fisica e Astronomia
Corso di Laurea Magistrale in Fisica

Search for a diffuse flux
of cosmic neutrinos in the shower channel
with the ANTARES telescope

Relatore:

Prof.ssa Annarita Margiotta

Correlatore:

Dr. Luigi Antonio Fusco

Presentata da:

Federico Versari

Anno Accademico 2015/2016

Contents

Contents

Abstract

ANTARES è il più grande telescopio di neutrini sottomarino in funzione al momento. Si trova nel Mar Mediterraneo, 40 km a largo di Tolone, Francia, ed è composto da 885 fotomoltiplicatori disposti lungo linee verticali ancorate sul fondo marino a 2475 m di profondit. L'obiettivo principale di ANTARES è l'osservazione di neutrini di alta energia di origine astrofisica.

Il telescopio di neutrini IceCube, situato al Polo Sud, ha misurato negli ultimi anni un eccesso di neutrini di altissima energia ($>$ TeV) rispetto ai fondi atteso. Questo flusso proviene da sorgenti sconosciute e non risolvibili come sorgenti individuali. ANTARES può investigare questo eccesso sfruttando la complementarietà del suo campo di vista e le ottime capacit di ricostruzione direzionale ed energetica del rivelatore.

Una ricerca di flussi diffusi di neutrini cosmici su tutto il cielo è presentata in questa tesi. In particolare si sfruttano gli eventi di tipo sciame per cui è possibile ottenere un'ottima risoluzione energetica, che permette di rigettare in maniera precisa il fondo dato da eventi atmosferici. Una catena di tagli per la selezione di un campione di eventi sufficientemente puro è definita nell'analisi. L'intero campione di dati raccolti da ANTARES tra il 2007 ed il 2013 è stato analizzato per questa analisi, producendo un osservazione di 7 eventi su un fondo atteso di 5±2.

Introduction

Neutrino astronomy is the youngest branch of astroparticle physics. TeV neutrino astronomy is even younger, since only recently the IceCube detector provided the first ever observation of high energy neutrinos of cosmic origin. This has opened a new window of observation on the Universe.

The energy output of astrophysical objects in photons can be only marginal, and much information can then be lost on the mechanisms at work. A large amount of energy can be given to charged and neutral particles. In particular, neutrinos produced close to or inside astrophysical objects can provide fundamental information on the objects themselves. A few neutrino events from the Supernova SN1987A has given us an unprecedented insight on the explosion of massive stars. Analogously, observing neutrinos from more energeti objects could answer many questions on the way these objects work.

The observation of neutrinos of extra-terrestrial origin can solve a fundamental question in astroparticle physics: the origin, the sources and the acceleration mechanisms of charged cosmic rays. Since neutrinos could be produced in the dense environment surrounding the acceleration site, they can directly point to the cosmic ray source and accelerator.

A possible way to detect high energy neutrinos using huge volumes of transparent natural material such as ice or sea water was proposed by Markov in 1960. High energy neutrinos undergoing weak interactions with one of the nucleons of the medium would produce charged particle. Cherenkov photons can then be detected by a lattice of photomultipliers. Given the low cross section of νN interactions and the predicted astrophysical neutrino fluxes, the typical size of the detector should be of the order of km^3.

The ANTARES neutrino telescope is a three-dimensional array of photomultipliers distributed over 12 lines, installed in the Mediterranean Sea. The detector has been operated in partial configurations since March 2006 and was completed in May 2008. It is taking data continuously since then. The main goal of the experiment is to search for high energy neutrinos from astrophysical sources.

In this thesis a search for a diffuse flux coming from unresolved neutrino sources in the whole sky with the ANTARES neutrino telescope is presented. In particular, the shower channel is exploited. This channel provides the best energy resolution of these

searches, improving the possibility to reject atmospheric background.

The structure of this thesis is as follows. A general overview of the knowledge of cosmic rays and neutrino astrophysics in given in Chapter 1. In Chapter 2 a description of diffuse neutrino fluxes is provided, specifically pointing to the observation of the cosmic diffuse flux from the IceCube Collaboration. Then, in Chapter 3, the ANTARES telescope is presented. In Chapter 4 the Monte Carlo simulations and analysis tools used for the analysis are described. Finally, Chapter 5 reports on the search for a diffuse flux of showering neutrino events, providing an analysis of the complete ANTARES data sample.

Chapter 1

Neutrino astronomy

Introduction

Neutrinos are neutral leptons and the lightest known massive particles. They undergo only weakly interactions and this allows them to act as a unique messenger from far and dense astrophysical objects. In fact they can traverse the interstellar matter without interacting and being deflected by magnetic fields. Neutrinos can then be used to look deep in space and offer a complementary view to photons. However, these properties make their detection challenging.

Following an idea by Markov [1], large natural masses of ice or water can be made sensitive to neutrinos by using optical detectors to collect the Cherenkov photons emitted along the path of the relativistic charged particles produced in neutrino interactions. A new window of observation can then be opened to the Universe.

1.1 Cosmic Rays

The existence of a cosmic radiation was discovered in 1912 when Victor Hess [2], using golden electrometers in free balloon flights, found that the intensity of natural radiation increases with altitude.

Before particle accelerators, cosmic rays (CR) represented the only source of high energy particles. Even now, the energy reached by CR interactions is several orders of magnitude larger than that accessible with accelerators like the LHC.

Up to now, the origin and the acceleration mechanisms of CRs are not completely understood. Direct measurements of the CR composition show that they are mostly protons (90 %) and helium nuclei (about 9 %) with a small amount of heavier nuclei (1 %) and a little fraction of electrons and γ rays.
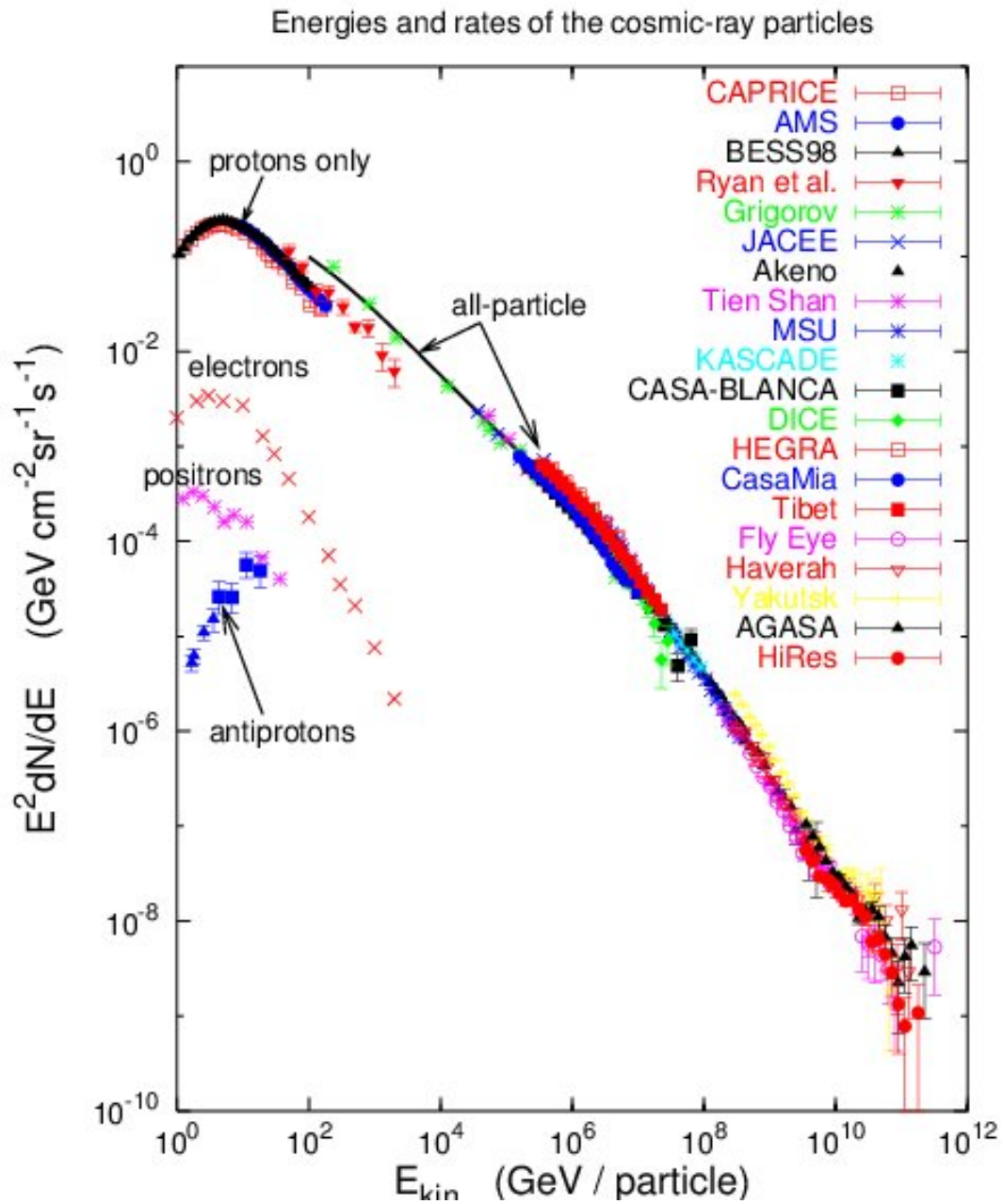
Figure 1.1: Cosmic ray energy spectrum measured by different experiments. It is multiplied by a E^2 factor to emphasise the various shapes. Picture taken from [3].
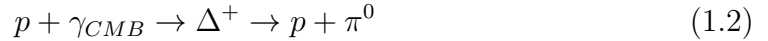
1.1 Cosmic Rays

The primary CR energy spectrum can be described as a power law:

$$\frac{dN}{dE} \sim E^{-\gamma} \qquad (1.1)$$

where E is the CR energy and γ the spectral index. As shown in figure 1.1, at least four regions can be identified in the spectrum, characterised by different values of the spectral index:

1. For CR energies up to $E \approx 3 \cdot 10^{15}$ eV, $\gamma \approx 2.7$. CRs up to this energy (usually called the *knee* region of the spectrum) are considered of Galactic origin and their acceleration mechanisms can be explained with the so-called Fermi mechanism [4, 5], most likely taking place within Supernovae Remnants (SNRs) in our Galaxy;

2. $3 \cdot 10^{15}$ eV $< E < 3 \cdot 10^{19}$ eV: the spectral index $\gamma \approx 3.1$. In this energy range a transition from Galactic to extra-Galactic sources is expected;

3. $\gamma \approx 2.7$ for energies above $E \approx 3 \cdot 10^{19}$ eV. For energies larger than $3 \cdot 10^{19}$ eV, the *ankle*, a flottening of the energy spectrum is present and the spectral index is again ~ 2.7;

4. at about $6 \cdot 10^{19} eV$ a spectral cutoff is expected because of the so-called *Greisen-Zatsepin-Kuz'min* (GZK) [6, 7] effect, where CRs interact with the Cosmic Microwave Background (CMB) photos by the Δ^+ resonance.

$$p + \gamma_{CMB} \rightarrow \Delta^+ \rightarrow p + \pi^0 \qquad (1.2)$$

or

$$p + \gamma_{CMB} \rightarrow \Delta^+ \rightarrow n + \pi^+ \qquad (1.3)$$

The arrival directions of CRs at the top of the atmosphere are distributed isotropically because of the Galactic ($\sim 4~\mu$G) and extra-Galactic ($\sim$ nG) magnetic fields, which bend the trajectories of charged particles. Only very high energy charged CRs point back to their sources. The Larmor radius describing the bending of charged particles in magnetic fields is defined as:

$$R_L = \frac{mv_\perp}{|q|B} \qquad (1.4)$$

where m is the mass of the particle of charge q, $v_\perp$ the perpendicular component of the velocity respect to the magnetic field $\vec{B}$. For a proton, the R_L is comparable to the Milky Way thickness ($\sim$ 200 pc, where 1 pc = 3.26 light-years) only for energies above 10^{18} eV. Thus CRs below this energy are strongly deflected and confined in the Galaxy, where they can scatter in magnetic fields inhomogeneities, being deflected several times.

1.2 Neutrino sources and CRs acceleration

Neutrinos can be produced in a variety of objects and processes in the Universe. The expected spectrum could cover several orders of magnitude in the energy and flux. The first ever observed extra-terrestrial neutrinos were solar neutrinos, produced in nuclear fusion reactions, in the core of the Sun. These neutrinos have an energy ranging from a few hundred keV up to a few MeV.

The first and up to now only proven source of neutrinos from outside our Solar System is the supernova SN1987A, which took place on February 23rd 1987. In this occasion three neutrino experiments, Kamiokande II, IMB and Baksan [8, 9, 10], independently measured a neutrino burst which had been related to that source, in the energy range of a few MeV. An overview of the possible neutrino sources above 100 GeV is presented in the following.

1.2.1 Atmospheric neutrinos

When cosmic rays enter the Earth's atmosphere they collide with atmospheric nuclei (mainly nitrogen and oxygen) and produce cascades of secondary particles. Up to ~ 100 TeV, muons and neutrinos are produced mainly by decays of charged pions and kaons in the cascade and their spectra are related by the kinematics their decays:

$$\pi \rightarrow \mu\nu \tag{1.5}$$

$$K \rightarrow \mu\nu \tag{1.6}$$

Additional lower energy neutrinos are produced by the consequent muon decays:

$$\mu \rightarrow e + \nu_e + \nu_\mu \tag{1.7}$$

The corresponding muon neutrinos flux is usually referred to as the *conventional atmospheric neutrino flux* and its intensity is expressed, for a given primary spectral index γ_p, as:

$$\frac{d\Phi_\nu}{dE_\nu d\Omega}(E_\nu, \theta) = A_\nu \cdot E_\nu^{-\gamma_p} \cdot \left(\frac{1}{1 + \frac{aE_\nu}{\epsilon_\pi}cos(\theta)} + \frac{B}{1 + \frac{bE_\nu}{\epsilon_K}cos(\theta)} \right) \ [\mathrm{cm}^{-2} \cdot \mathrm{s}^{-1} \cdot \mathrm{sr}^{-1} \cdot \mathrm{GeV}^{-1}] \tag{1.8}$$

The *scale factor* A_ν, the *balance factor* B (which depends on the ratio of muons produced by kaons and pions) and the a, b coefficients are parameters which can be derived from Monte Carlo computation, numerical approximations or from experimental data. The quantity ϵ_i (the *characteristic decay constant*) corresponds to the energy at which the hadron interaction and decay lengths are equal and its value for pions and kaons are, respectively:

$$\epsilon_\pi = 115 \ \mathrm{GeV} \tag{1.9}$$

$$\epsilon_K = 850 \text{ GeV} \tag{1.10}$$

An analytic description of the neutrino spectrum above 100 GeV is given by Volkova [11]. Conventional atmospheric neutrino fluxes are also provided by the Bartol [12, 13] and Honda [14] calculations. The expected power-law spectrum of conventional atmospheric neutrinos for $E_\nu \gg \epsilon_\pi, \epsilon_K$ can be approximated with:

$$\frac{d\Phi_\nu}{dE_\nu}(E_\nu) = A'_\nu \cdot E_\nu^{-\gamma_\nu} \tag{1.11}$$

where:

$$\gamma_\nu \simeq \gamma_p + 1 \tag{1.12}$$

The major uncertainties in the calculations of the atmospheric neutrino flux arise from uncertainties on the composition, absolute normalisation and slope γ_p of the primary cosmic ray spectrum, as well as the treatment of hadronic interactions in the particle cascades in the atmosphere. The uncertainty on the normalisation of the conventional atmospheric neutrino flux is estimated to be at the level of 25-30% [14, 15].

Charmed hadrons, produced by interactions of primary cosmic rays with air nuclei, have a much shorter lifetime, approximately 5 to 6 orders of magnitude smaller than pions and kaons. This allows them to decay instead of interact, therefore producing a harder neutrino energy spectrum (*prompt neutrino flux*). There is a significant variability in the different calculations of the prompt neutrino fluxes [16, 17, 18], depending on the modeling of the hadronic interactions, the choice of gluon distributions and the renormalisation and factorisation scales.

1.2.2 Galactic ν sources

- *Galactic centre (GC)*: The center of the Milky Way, is a site of great interest for a neutrino telescope placed in the Northern Hemisphere, because of the shielding provided by the Earth to cosmic rays. A supermassive black hole is hosted there and γ-ray emission has been detected [19]. According to some models [20], this γ emission could be accompanied by high-energy neutrino production.

- *Fermi-Bubbles*: Above and below the center of the Milky Way, multiple observatories have provided hints of a diffuse radio, microwave, X-ray and γ-ray emission [21]. An emission of neutrinos might be accompanying this γ emission if this is due to the interaction of accelerated CRs with the interstellar medium.

- *Supernova Remnants (SNR)*: SNRs are the main candidates for acceleration of Galactic CRs. After a supernova, the expanding material shell produces a shock-wave that, by the Fermi mechanism [4, 5], can accelerate CRs up to $300 \times Z$ TeV. If the end product of the SN is a Neutron Star (NS), the particles may undergo further

acceleration because of the presence of strong and variable magnetic fields. Since CRs are accelerated at high energies, their interaction with the ambient medium can produce neutrinos along with γ-rays [22].

- *Pulsar Wind Nebulae (PWN)*: In the presence of strong magnetic fields near a rotating NS, charged particle can be accelerated by strong electric fields through Faraday's law. This can enhance the CR energy up to 10^{18} eV. Neutrinos can be produced at these sites in the same way as for common SNRs [24].

- *Microquasar*: Microquasars are binary systems emitting X-rays and showing jets in the radio band. Because of the presence of relativistic jets, these objects could accelerate charged particles up to about 10^{16} eV. Neutrino production is foreseen from the interaction of jets with the ambient medium [23].

1.2.3   Extra-galactic ν sources

- *Active Galactic Nuclei (AGN)*: Galaxies hosting a super-massive black hole in their centre can show a strong photon emission from jets. The central black hole accretes surrounding matter and releases electromagnetic energy at different wavelengths. According to some models, the presence of jets can be related to CRs acceleration and hence neutrino production [25]. AGNs are the main candidates for the acceleration of CRs to the highest energies.

- *Gamma Ray Burst (GRB)*: Short-time emissions of high energy photons are observed from extra-Galactic sources. Models foresee that this emission is caused by the outburst of jets from a central engine in a collapsing environment (large mass supernovae or merging binary systems). The presence of jets in a dense environment might allow the acceleration of CRs and consequently the production of HE neutrinos [26]. Requiring a space and time coincidence of these phenomena with neutrino detection would strongly reduce the background.

- *Exotic source: Dark Matter (DM)*: The existence of dark matter is supported by experimental and cosmological evidence. A possible DM candidate are WIMPs (Weakly Interacting Massive Particles). Self annihilation of WIMPs, gravitationally trapped inside massive objects (the Earth centre, the Sun, the Galactic Centre), can produce a neutrino signal. This flux can be detected by the observation of a directional excess where the expected neutrino background is low [27].

1.3   Neutrino physics

Neutrinos only interact via *weak interactions* (W.I). W.I. are short-range and mediated by the exchange of charged ($W^{\pm}$) and neutral (Z^0) massive bosons. The interactions

between neutrinos and matter can be classified in two types, depending on the mediator:

- *Neutral current (NC)*: The interaction is mediated by the neutral boson Z^0. The neutrino in the final state is identical to the incoming one and no charged lepton is produced. This can be generally represented by the reaction:

$$\nu_f + N \rightarrow \nu_f + X \tag{1.13}$$

where ν_f is a neutrino of flavour f, N is a nucleon and X is a generic final hadronic state.

- *Charged current (CC)*: The interaction is mediated by the charged bosons $W^{\pm}$. In the final state a lepton as the same flavour of the interacting neutrino is produced

$$\nu_l + N \rightarrow l^- + X \tag{1.14}$$

$$\overline{\nu}_l + N \rightarrow l^+ X \tag{1.15}$$

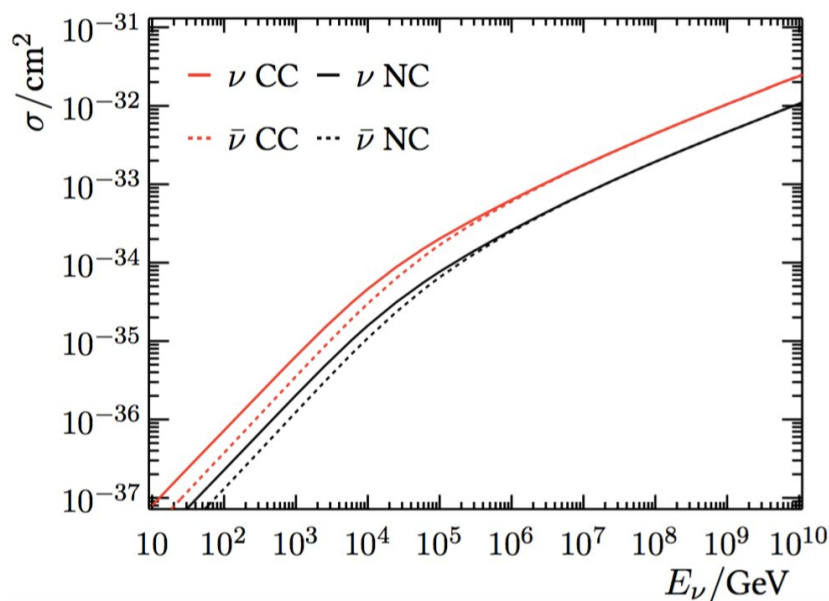Figure 1.2 shows the energy dependence of the neutrino cross section for CC and NC interactions.

Figure 1.2: Energy depence of neutrino and antineutrino cross-section in scattering processes. Figure taken from [28].

1.3.1   Neutrino oscillations

Suggested for the first time by Pontecorvo in 1957 [29], neutrino oscillations are a phenomenon according to which massive neutrinos can change their identity as they travel along their path. Oscillations from one flavour to another are due to the fact that the *weak interaction eigenstates* (ν_α) aren not *mass eigenstates* (ν_i), but a combination of them:

$$|\nu_\alpha\rangle = \sum_{i=1}^{3} U_{\alpha,i}|\nu_i\rangle \tag{1.16}$$

where α represents the three flavour (e, μ, τ) and i runs from 1 to 3 and represents the mass eigenstates. Considering only two neutrino states, the oscillation probability between them as a function of the source distance is given by:

$$P_{\alpha,\beta} = sin^2\left(2\theta_{\alpha,\beta}\right) \cdot sin^2\left(1.27\frac{L}{E}\Delta m^2\right) \tag{1.17}$$

where:

- $\theta_{\alpha,\beta}$: neutrino mixing angle;

- $\Delta m^2 = m_\alpha^2 - m_\beta^2$ [eV];

- L [m]: distance between the neutrino source and the detector;

- E [MeV]: neutrino energy;

1.4   Neutrino telescopes

As proposed by Markov [1], a neutrino telescope is a 3-dimensional array of optical sensors, installed at a great depth under water or ice. These sensors can detect the Cherenkov photons given by the products of neutrino interactions in the surroundings of the instrumented apparatus.

1.4.1   Cherenkov light emission

CC and NC neutrino interactions can produce electromagnetic and hadronic showers or a track. These are mainly made of relativistic charged particles. When a charged particle travels faster than the speed of light in an insulator, Cherenkov [30] photons are emitted. Charged particles polarise the molecules along their trajectory and radiation is emitted when molecules depolarise.
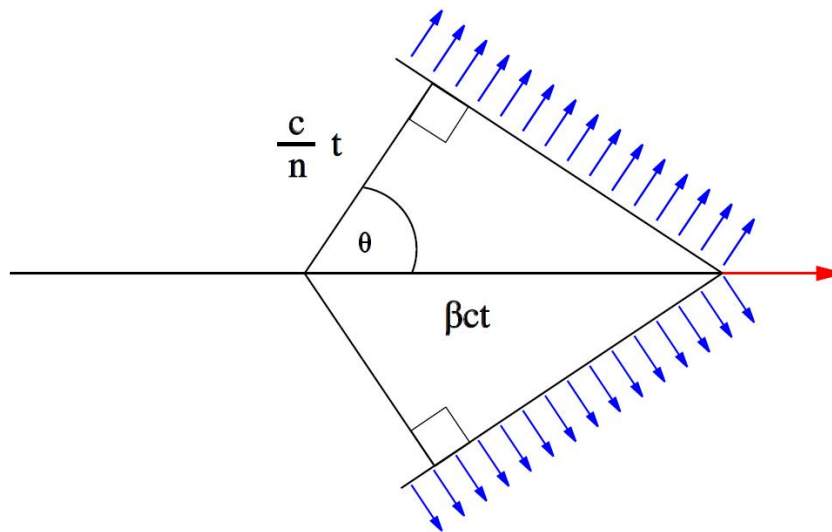
Figure 1.3: Illustration of the Cherenkov cone.

This light is generated in a cone with a characteristic angle θ_c:

$$cos(\theta_c) = \frac{1}{\beta n} \qquad (1.18)$$

$$\beta = \frac{v}{c} \qquad (1.19)$$

where n is the refractive index of the insulator.

For highly relativistic particles ($\beta \approx 1$) in sea water ($n \approx 1.36$), the Cherenkov cone has an opening angle of about 42 degrees. The number of Cherenkov photons N emitted per unit wavelength interval $d\lambda$ and unit travelled distance dx by a charged particle of charge e is given by:

$$\frac{d^2 N_\gamma}{dx d\lambda} = \frac{2\pi}{137\lambda^2} \cdot \left(1 - \frac{1}{n^2\beta^2}\right) \qquad (1.20)$$

Cherenkov emission is mostly in the visible and UV wavelengths ($300 \div 600$ nm) and the mean number of Cherenkov photons emitted is about $3.5 \cdot 10^4$ m^{-1}.

1.4.2 Event topologies

Three event topologies can be observed in a neutrino telescope: track events, shower events and *double-bang* events.

Tracks events

When a muon neutrino interacts via CC, a muon is produced. The Cherenkov photons emitted along the muon path allow the reconstruction of the muon track direction.
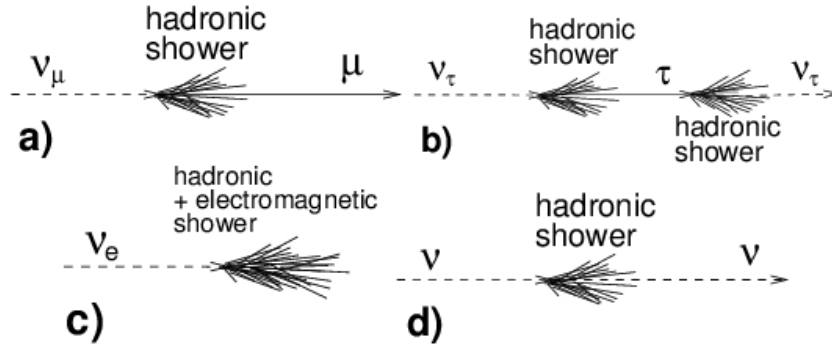
Figure 1.4: Event topologies for different neutrino flavours and interactions. Figure taken from [31].
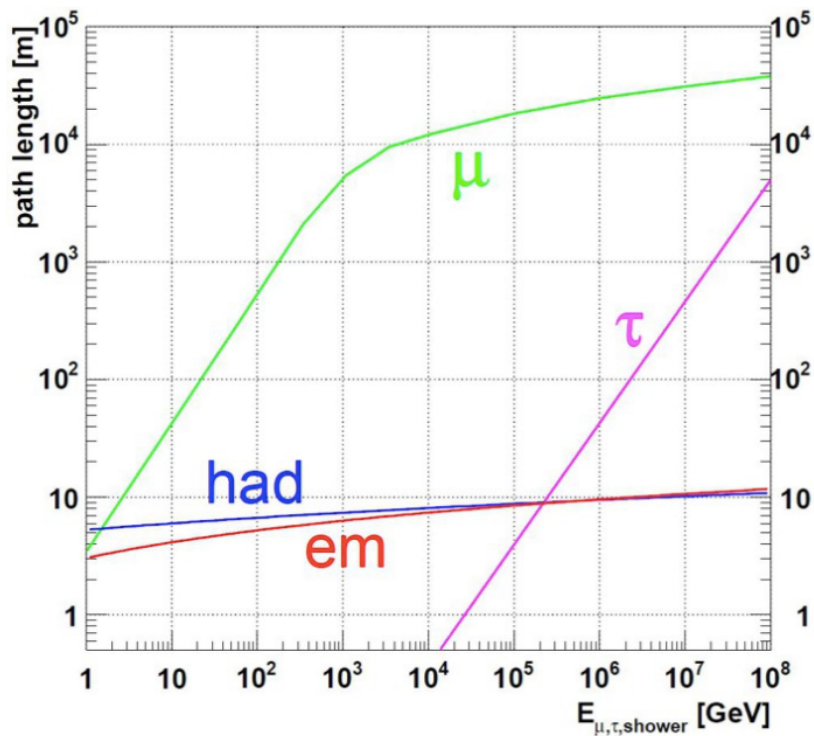

Figure 1.5: Longitudinal ranges of different event topologies. The plot shows the range of muon and tau lepton tracks and the length of hadronic and electromagnetic cascades as function of the particle/shower energy. Figure taken from [32].

Analogously the amount of the Cherenkov light emitted can be used to estimate the released energy. The angle between the muon and the neutrino directions is:

$$\theta_{\nu\mu} \approx \frac{0.6^o}{\sqrt{E_\nu(TeV)}} \tag{1.21}$$

and this channel provides the best performance for pointing.

Muons lose energy because of ionisation, bremsstrahlung, photo-nuclear interactions and pair production. The muon range, defined as the distance that the particle of energy E_μ, can travel before reaching the detection threshold E_μ^{thr}, ranges from a few hundred up to several thousand meters as shown in figure 1.5. This largely increases the effective volume of the detector since neutrino interactions happening far away from the instrumented volume can still be detected. However for the majority of high energy events, the interaction vertex is far outside the detector. As a consequence only part of the muon track is directly observed in the detector. This limits the capabilities of neutrino energy reconstruction for track-like events.

Shower events

Hadronic and electromagnetic showers are produced when a neutrino (of every flavour) interacts via NC or an electron neutrino interacts via CC. As long as the charged particles in the showers are above the Cherenkov threshold, light is emitted. The topology of a shower can be described as a function of its longitudinal and lateral extension.

An electromagnetic (EM) cascade is produced by a high-energy electron that radiates a photon via bremsstrahlung and the consequent pair production reactions. It has a longitudinal extension of few meters and its lateral extension is negligible compared to the longitudinal one. Such a shower is short compared to the spacing between the PMTs in a neutrino telescope: EM showers represent to a good approximation, a point source of Cherenkov photons. For this reason the angular resolution for shower events is worse with respect to that obtained for track events.

Hadronic showers, produced in NC interactions, show the same features as E.M. cascades, even though they are effected by more important event-by-event fluctuations. The most common secondary particles in this kind of cascade are pions, kaons and nucleons. Muons produced in pion decays usually leave the shower producing few photons, so they contribute significantly to the fluctuations. Figure 1.5 show that the longitudinal profile of hadronic showers is very similarly to the EM one. So, even if there are many possible differences between the two kind of cascades, they are not distinguishable in large volume neutrino detectors.

Due to the fact that all the shower particles are contained within a few meters from the interaction vertex, all Cherenkov photons are emitted almost isotropically along the shower axis. For this reason a calorimetric measurement of the shower energy can be

performed. Only a limited amount of the shower energy is in fact taken away by neutral particles that do not emit any light.

Table 1.1: Main τ branching ratios from [33].

Channel	BR (%)
$\pi^-\ \pi^0\ \nu_\tau$	**25**.4940 ± 0.0893
$e^-\ \overline{\nu_e}\ \nu_\tau$	**17**.8174 ± 0.0399
$\mu^-\ \overline{\nu_\mu}\ \nu_\tau$	**17**.3936 ± 0.0384
$\pi^-\ \nu_\tau$	**10**.8165 ± 0.0512
$\pi^-\ 2\pi^0\ \nu_\tau$	**9**.2595 ± 0.0964
$2\pi^-\ \pi^+\ \nu_\tau$	**8**.9870 ± 0.0514
$2\pi^-\ \pi^+\ \pi^0\ \nu_\tau$	**2**.7404 ± 0.0710

Double-bang events

When a tau neutrino interacts via CC ,it produces a τ lepton. Tauons have a short lifetime ($2.9 \cdot 10^{-13}s$) and decay producing various particles, with Branching Ratios (BR) reported in table 1.1. This peculiarity allows the identification of τ events. In fact for large enough τ energies, the Lorentz factor can be large the τ can produce a visible track before the decay. Overall, a shower is produced at the interaction vertex (first _bang_) and another one at the tauon decay point (second _bang_), connected by a track-like signature. Such a double bang event can be observed in a large volume neutrino telescope only if the τ energy is in the order of 1 PeV or larger.

1.4.3   Current and future neutrino telescopes

Different options have been investigated for the construction of neutrino telescopes. The properties of water and ice, of absorbing and scattering photons, significantly affect the performance of the detector in obtaining a high quality reconstruction of the neutrino properties. Neutrino telescopes can then be classified according to the medium in which they are immersed. In general, ice is more transparent than water but the presence of dust and air bubbles trapped in it, causes a larger diffusion of photons and a degradation of the reconstruction performance.

An overview of past, present and future of neutrino telescopes, classified according to the medium and arranged chronologically is presented in the following.

Under-water neutrino telescope

Water, as a medium for high energy neutrinos detection, was investigated either in the sea (or ocean) and in deep lake. The first project ever was DUMAND [34], operated from 1976 until 1995 in the Pacific Ocean offshore Hawaii Islands at a depth of about 4800 m; all the subsequent projects took advantage of the experience coming from it.

A neutrino telescope has been built in the Lake Baikal, Russia, at a depth of ~ 1800 m [35]. The first test detection units were deployed in the early nineties and, with these, it was possible to make a first search for high energy neutrinos [36]. The detector is currently being expanded to a Gton volume [37].

At the moment, the center of gravity of the research in under-water neutrino telescopes is the Mediterranean Sea. The presence of large abyssal planes, with depths ranging from 2500 to 4500m and low deep sea current favours this development. Three sites have been studied, investigated and used to build three detectors:

- The NESTOR Collaboration [38] investigated the Greek site, off-shore Pylos, Peloponnese, deploying some test units and measuring the muon flux at a depth of more than 3000 m.

- The ANTARES telescope [39], figure 1.6, the detector on which this thesis is focused, is located at a depth of about 2500 m 40 km off-shore Toulon, France. Until next year (2017), when the KM3NeT [40] will exceed its size and performance, ANTARES will remain the largest under-water neutrino telescope and the largest neutrino detector in the Northern hemisphere.

- KM3NeT is a future research infrastructure comprising the ARCA and ORCA projects. The former will be located about 100 km off-shore from the coast of Portopalo di Capo Passero, Sicily, Italy at a depth of 3500 m. The latter will be located close to the ANTARES site about 10 km apart from it. The ARCA detector is designed for the investigation of high energy neutrino astrophysics and the search for the sources of cosmic neutrinos. The ORCA detector is optimised for the study of low energy neutrino oscillation physics and for the measurement of the neutrino mass hierarchy. At the moment the KM3NeT project is in its Phase-I construction stage [40].

Under-ice neutrino telescope

The Antartic Ice shell can be exploited to build a neutrino telescope. Starting from the experience of the AMANDA [41] detector, its successor IceCube [42], depicted in figure 1.7, is currently the largest neutrino telescope in the World. It is located at the geographic South Pole, at the permanent Amudsen-Scott Pole Station. IceCube comprises an array of 5,160 Digital Optical Modules (DOMs) deployed on 86 strings at a depth of
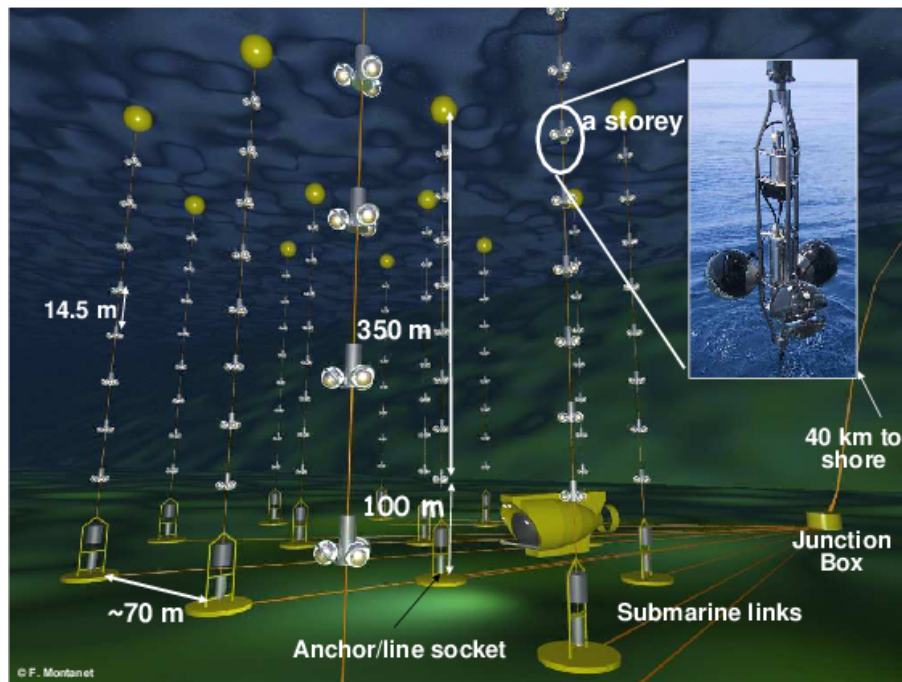
Figure 1.6: Schematic view of the ANTARES detector taken from [31].

1.5-2.5 km below the surface just above the bedrock in the clear, deep ice. High quantum efficiency PMTs are used in a denser sub-array located in the center of the detector. This sub-array, called DeepCore, enhances the sensitivity to low energy neutrinos, especially for neutrino oscillations studies. Finally, a surface CR detector, called IceTop, completes the IceCube Observatory. The total instrumented volume is about one cubic kilometre. The first observation of cosmic neutrinos, obtained by the IceCube Collaboration, will be described in chapter 2.
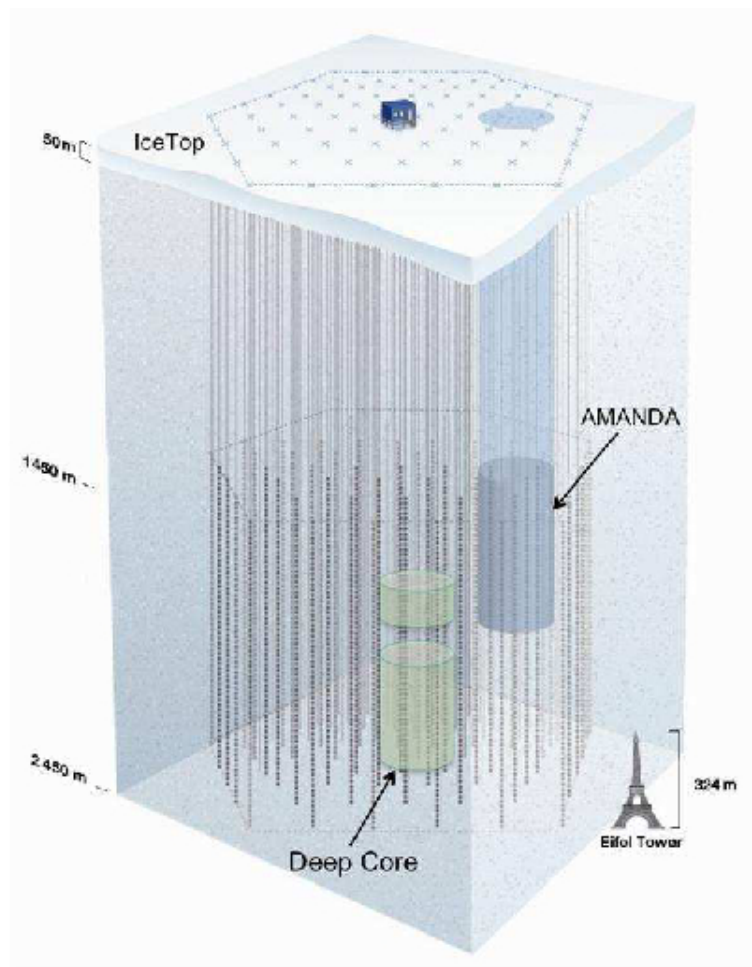
Figure 1.7: Schematic view of the IceCube detector taken from [31]

Chapter 2

Diffuse fluxes of cosmic neutrinos

The detection of an individual neutrino source would be the best way to identify and characterise a CRs accelerator. An alternative way to prove the existence of cosmic neutrino sources is the measurement of a diffuse all-sky flux, without using any directional information. This cosmic flux is expected from unresolved individual sources, that are too faint to produce a detectable point source signal. As cosmic neutrinos are expected to have an energy spectrum harder than the atmospheric one, this kind of analysis is performed by looking for an excess of high energy events.

2.1 Diffuse neutrino fluxes models

Many theoretical models describe the possible neutrino diffuse flux. Upper bounds can be derived from the observation of the diffuse flux of gamma-rays and of ultra high energy cosmic rays (UHECRs).

High energy gamma-rays are produced in astrophysical acceleration sites from the decay of neutral pions. The observed energy of these γ-rays ranges from 1 MeV to 100 GeV and a diffuse background above 30 MeV was measured by EGRET [45] experiment as:

$$E^2 I_\gamma(E) = (1.37 \pm 0.06) \cdot 10^{-6} \ [\text{GeV} \cdot \text{cm}^{-2} \cdot \text{sr}^{-1} \cdot \text{s}^{-1}] \tag{2.1}$$

This flux has not been associated to any known source and might be related to CRs accelerated by faint sources, interacting through their propagation. Neutrinos from the decay of charged pions produced along with these π^0 will escape from the source without interacting and a neutrino flux could be related to the same γ diffuse excess.

An analogous discussion can be done for CRs. When the Fermi acceleration mechanism takes place, protons are accelerated and magnetically confined near the source. Through photo-production interactions with the radiation fields, neutrons are produced. They can escape from transparent sources and decay into cosmic protons outside the the host accelerator. In this way a similar bound can be obtained from the measured flux
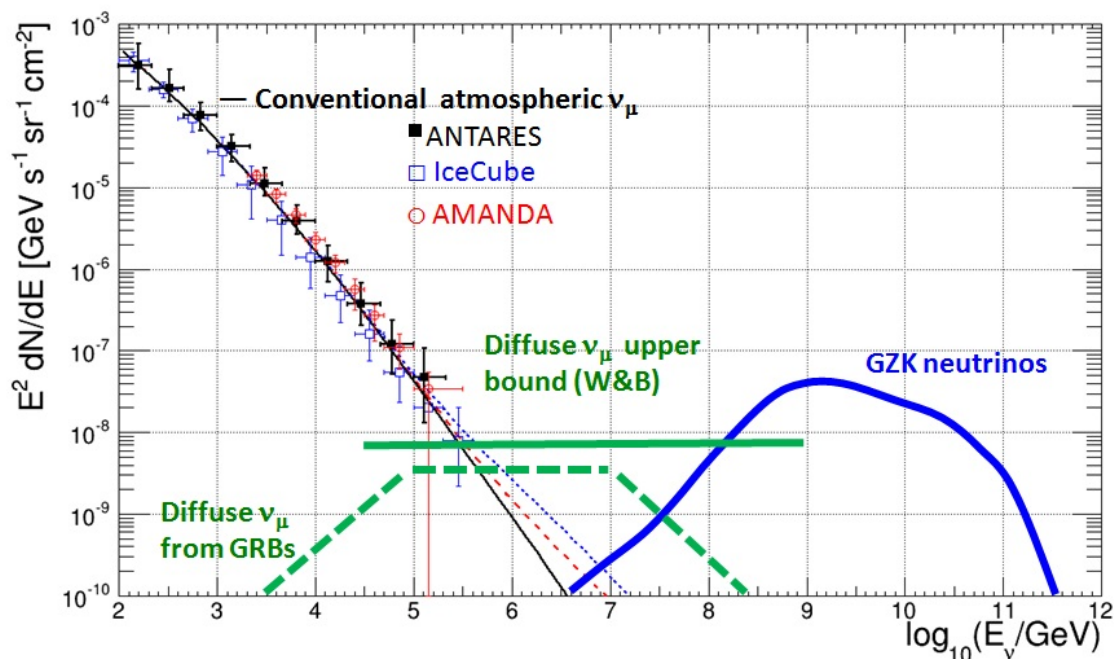
Figure 2.1: Expected neutrino fluxes from different diffuse cosmic models and the atmospheric neutrino background. The points represent the measurements of atmospheric $\nu_\mu + \overline{\nu}_\mu$ flux as a function of the energy by three experiments, in particular ANTARES data are taken from [43]. The black line is the expected conventional flux; the dashed line includes the contribution from two models of prompt neutrinos from charmed mesons decay. The horizontal full green line is the WB upper bound, the dashed green line is the upper bound for ν_μ produced by GRBs and the blue line indicated the possible contribution of neutrinos produced by the GZK model. Picture taken from [44].

of CRs of extragalactic origin. However, some additional factors must be considered: in particular the production kinematics, the opacity of the source to neutrons and the effect of propagation must be analysed. Large uncertainties affect the latter because it strongly depends on galactic evolution and on the poorly-known magnetic fields in the Universe.

2.1.1 The Waxman-Bahcall upper bound

The Waxman-Bahcall (WB) upper bound [46] is computed by taking into account the CRs observations at $E_{CR} \sim 10^{19}$ eV to constrain the diffuse neutrino flux. In this computation of the upper bound, several hypotheses are made: that neutrinos are produced by interaction of protons with ambient radiation or matter; that the sources are transparent to high energy neutrons; that the $10^{19} eV$ CRs produced by neutron decay are not deflected by magnetic fields; finally (and most important) that the spectral shape of CRs up to the GZK cutoff is:

$$\frac{dN}{dE} \propto E^{-2} \tag{2.2}$$

as typically expected from the Fermi acceleration mechanism.
The upper limit obtained with this assumptions is:

$$E_\nu^2 \frac{d\Phi}{dE_\nu} < 1.5 \cdot 10^{-8} \ [\text{GeV} \cdot \text{cm}^{-2} \cdot \text{sr}^{-1} \cdot \text{s}^{-1}] \tag{2.3}$$

Although this limit may be modified by hidden or optically thick sources for protons to pγ or pp(n) interactions, it represents the "reference" threshold to be reached by large volume neutrino detectors.
This bound dates back to 1998 and neutrino oscillations were not considered. Considering the effect of oscillations together with the new measurements of the UHECRs from the Pierre Auger Observatory (PAO) and Telescope Array (TA) Observatory, providing a lower flux than the one considered in 1998, the new upper bound is:

$$E_\nu^2 \frac{d\Phi}{dE_\nu} < 0.9 \cdot 10^{-8} \ [\text{GeV} \cdot \text{cm}^{-2} \cdot \text{sr}^{-1} \cdot \text{s}^{-1}] \tag{2.4}$$

2.2 Effect of neutrino oscillations

At present, neutrino oscillations represent a well-know phenomenon, observed in atmospheric, solar, accelerator and reactor neutrino experiment. This property of neutrinos also plays an important role in determining the flavour at Earth of neutrinos of cosmic origin. As already mentioned, high energy neutrinos are produced in astrophysical sources mainly through the decay of charged pions, in pγ, pp and pn interactions. Two muon

neutrinos are produced for each electron neutrino in the decay chain of each charged pion, assuming that the interaction length of π is larger then their decay length.

Tau neutrinos may also be produced by the decay of heavy charmed mesons. However, the high energy threshold and low cross-section for such reactions imply that the ratio of charmed meson to pion production is $\sim 10^{-4}$ and the fraction of $\frac{\nu_\tau}{\nu_\mu}$ a further factor ten smaller. Therefore, the ratio of the neutrino flavours at the source is expected to be:

$$\nu_e : \nu_\mu : \nu_\tau = 1 : 2 : 0 \tag{2.5}$$

Once they are produced, neutrinos freely stream in the Universe. In most situations, matter effects in oscillations [47, 48] can be neglected because high-energy cosmic neutrinos originate in regions of sufficiently low densities around the source. In addition, when distant sources are involved, the change in the flavour composition of the high-energy cosmic neutrinos due to vacuum mixing is essentially energy independent over the entire energy range relevant for observations. This occurs because the energy appears as argument of an oscillating function in the oscillation formulas, described in the first chapter, whose effects are averaged out for large L. Taking into account the considerations above and the long distances between the source and the Earth, the flavours of neutrinos arriving at Hearth will be completely mixed in the ratio:

$$\nu_e : \nu_\mu : \nu_\tau = 1 : 1 : 1 \tag{2.6}$$

2.3 The IceCube signal

The first observation of a cosmic neutrino signal has been reported by the IceCube collaboration in the High Energy Starting Events (HESE) analysis in 2013 [49, 50]. By means of a vetoing system, using the outer layers of the detector, atmospheric muons and neutrinos can be rejected in IceCube. This allows the selection of a cosmic neutrino sample coming from the whole sky. Indeed, above 100 TeV Earth absorption would strongly reduce the number of high energy neutrinos, thus reducing the possibility of observing an high energy neutrino signal as upward-going track-like events.

The IceCube HESE sample is dominated by downward-going events. This represents one of the main differences with respect to traditional diffuse flux analyses, where upward-going events are usually selected exploiting the natural shielding of the Earth from the atmospheric muon background.

Considering a cosmic neutrino flux which is equally distributed in the three neutrino flavours, looking for contained events favours the observation of showering events. For these events the angular resolution of IceCube is quite limited, being of the order of 20 degrees. Also for this reason, the sky-map of the HESE sample, reported in figure 2.3, does not show any significant excess with respect to the background expectations, even if an accumulation of events is present close to the Galactic Centre.
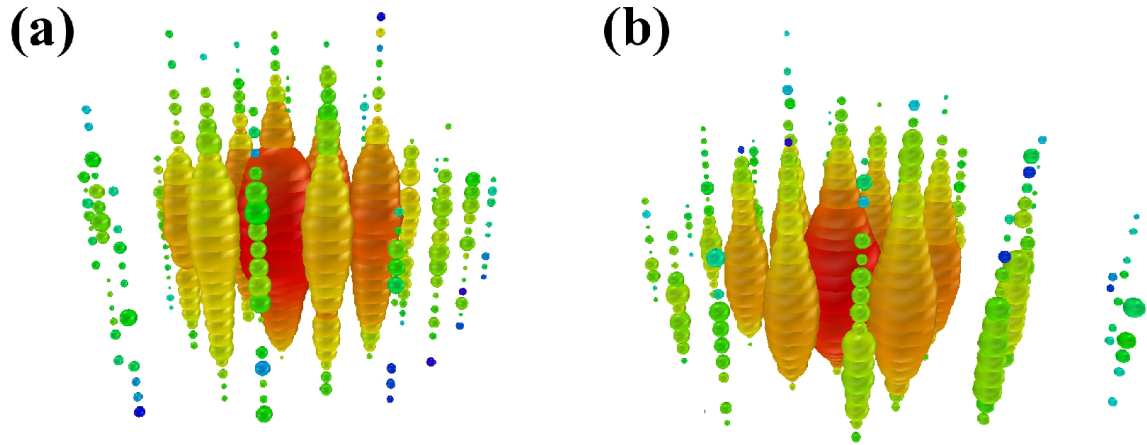
Figure 2.2: Event display of first two PeV neutrinos observed from IceCube called (**a**) *Bert* and (**b**) *Ernie*. Pictures taken from [49].
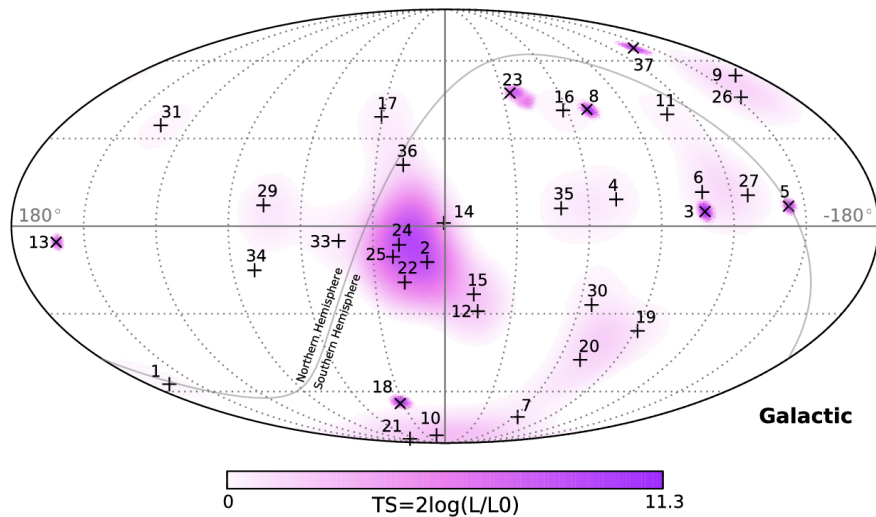

Figure 2.3: Arrival directions of the IceCube HESE event sample in galactic coordinates. Shower-like events (median angular resolution ~ 15 [deg]) are marked with + and those containing muon tracks (≤ 1 [deg]) with ×. Colors show the test statistic (TS) for the point source clustering test at each location. No significant clustering was observed. Picture taken from [50].

The zenith distribution is compatible with an isotropic flux; however, the neutrino rate from the Southern Sky is larger than that from the Northern Sky, hinting some possible anisotropy that can be related to the presence of the Milky Way in the Southern Sky. This possible excess has already been analysed with the ANTARES data strongly constraining this hypothesis [51].

The flavour composition of the cosmic neutrino signal has been analysed too. The data sample is consistent with equipartition in the three neutrino flavours [52]. Though the best fit composition at Earth is $(0 : 0.2 : 0.8)$, the limits are fully compatible with all possible source compositions.

The IceCube signal was initially fitted with an unbroken power law spectrum with spectral index equal to 2:

$$E_\nu^2 \frac{d\Phi}{dE_\nu} = (0.95 \pm 0.3) \cdot 10^{-8} \ [\text{GeV} \cdot \text{cm}^{-2} \cdot \text{sr}^{-1} \cdot \text{s}^{-1}] \tag{2.7}$$

even if also an $E^{-2.3}$ spectrum was compatible with the observed signal, mainly because of the absence of events above 2 PeV and the lack of an enhanced neutrino detection in the region of the Glashow resonance:

$$\overline{\nu}_e + e^- \rightarrow W^- \tag{2.8}$$

$$E_{\overline{\nu}_e}^{th} = 6.4 \ \text{PeV} \tag{2.9}$$

The absence of Glashow-resonance events would also hint to the presence of a cut-off in the spectrum at a few PeV.

The further extension of the IceCube sample and refinements of the analysis, in order to access energies of few tens of TeV, show a steepening of the energy spectrum. In the most recent publication, the best fit [52], done both on normalization and spectral index, is reported as:

$$\frac{d\Phi}{dE_\nu} = (2.3 \pm 0.4) \cdot 10^{-18} \left(\frac{E}{100 \ \text{TeV}} \right)^{2.6 \pm 0.15} \ [\text{GeV} \cdot \text{cm}^{-2} \cdot \text{sr}^{-1} \cdot \text{s}^{-1}] \tag{2.10}$$

in the energy range 25 TeV - 2.8 PeV, rejecting the E^{-2} hypothesis with a significance of 3σ. On the other hand, diffuse flux searches in the upward-going muon neutrino channel (Northern Sky for IceCube) report a 5.9σ excess with respect to the expected atmospheric backgrounds, compatible with a flux described by:

$$\frac{d\Phi}{dE_\nu} = \left(0.82_{-0.26}^{+0.30} \right) \cdot 10^{-18} \left(\frac{E}{100 \ \text{TeV}} \right)^{2.08 \pm 0.13} \ [\text{GeV} \cdot \text{cm}^{-2} \cdot \text{sr}^{-1} \cdot \text{s}^{-1}] \tag{2.11}$$

in the energy range 220 TeV - 8.3 PeV. An extremely high energy event with an estimated neutrino energy larger than 7 PeV is observed; this event has not been correlated yet to
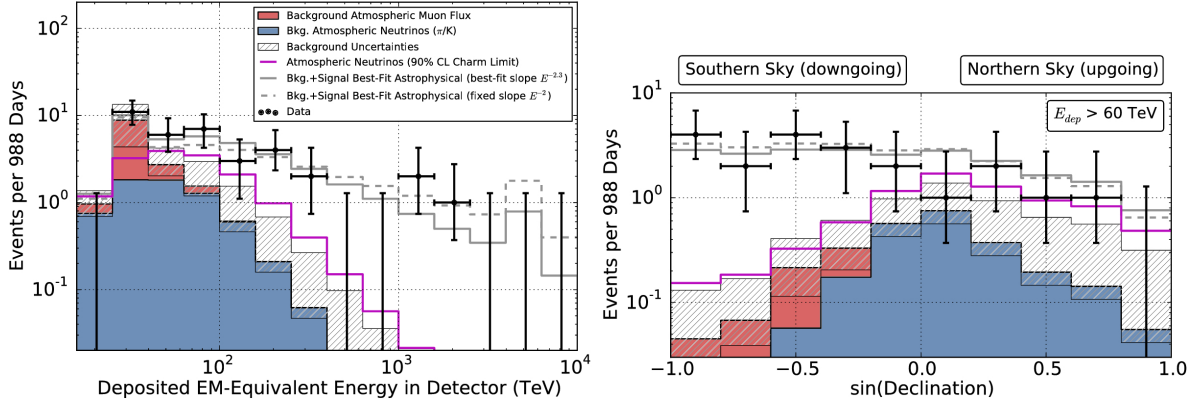
Figure 2.4: **Left**: Deposited energies of the IC observed events with predictions. **Right**: Arrival angles with $E > 60$ TeV. The increasing opacity of the Earth to high energy neutrinos is visible at the right of the plot. Pictures taken from [50].

any possible source and can be thus considered part of the diffuse, all-sky cosmic flux. This observation favours harder-spectra, no-cutoff hypotheses.

Some tension is present between the results from the HESE analysis and the diffuse, upward-going, tracks analysis. This contrast might be due to the existence of a neutrino emitting region in the Southern Sky, namely the Galactic Plane.

The detection of neutrinos from this region could produce an $E^{-2.5}$-like spectrum in the all sky analysis, which is biased in efficiency towards downward-going events. The analysis of upward-going tracks considers only the Northern Sky, thus extragalactic events which are expected to produce E^{-2}-like neutrino fluxes. Indeed it is usually expected that extragalactic cosmic ray accelerators, not opaque to their emission, would produce E^{-2}-like CRs and, consequently, neutrino energy spectra [46]. If absorption is present at the source, as in starburst galaxies, softer spectra should be expected [53]. A two components solution, Galactic plus extra-Galactic, for the IceCube observations could reasonably explain the signal [54].
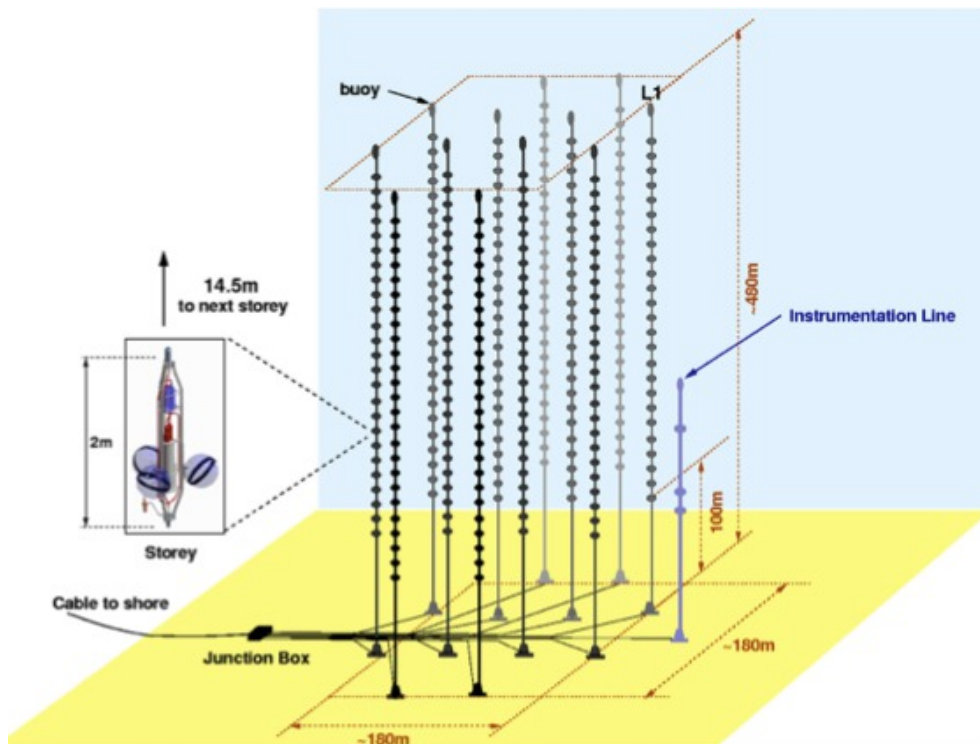
Chapter 3

ANTARES

Figure 3.1: Schematic view of the ANTARES detector.

ANTARES (**A**stronomy with a **N**eutrino **T**elescope and **A**byss environmental **RES**earch) is the largest and longest operated neutrino telescope in the Northern hemisphere. Its construction began in 2006 and it has been completed in 2008. It has been continuously taking data since then, and analysed data samples date back to 2007.

The ANTARES detector is located 40 km off-shore Toulon, France, at a depth of

2475 m on the Mediterranean seabed. Its location makes it sensitive to a large part of the Southern sky, including the Galactic Centre region, which contains many interesting astrophysical objects.

3.1 Design

Following Markov construction principle (§1.4), ANTARES is a 3-dimensional array of optical sensors [55]. It consists of 885 optical modules (OMs) distributed along 12 lines. Each line has 25 storeys, each storey consisting of a triplet of OMs with the only exception of the twelfth line, where the last sector (upper five storeys) is equipped with acoustic devices. The arrangement of OMs in space, described in §3.1.3, was optimised by means of simulations in order to have the best neutrino detection efficiency. The telescope is connected to the shore station, located in La-Seyne-Sur-Mer, with a 40 km-long electro-optical cable that provides the power supply of the detector and guarantees the transmission from/to shore.
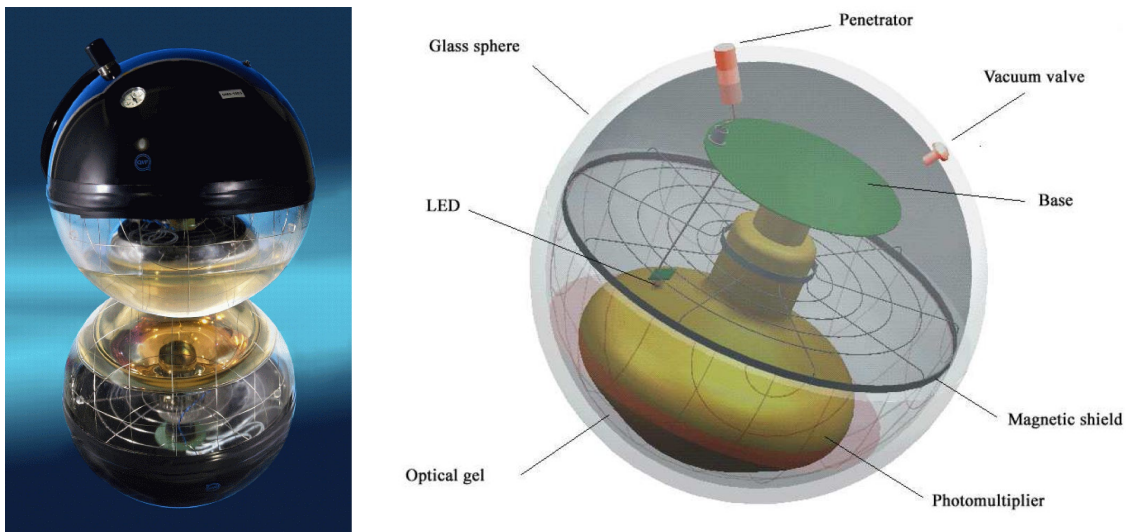
3.1.1 Optical module

Figure 3.2: **Left**: Photo of an Optical Module. **Right**: Schematic view of the Optical Module.

The Optical module (OM) is a pressure resistant 17-inch diameter glass sphere that contains a photomultiplier (PMT) to detect Cherenkov light. The PMT model was chosen during the research and development phase of the ANTARES project [55]. A

large detection area for each unit was required. Simulations showed that the geometrical area of the PMT should be larger than 500 cm^2 if a photocathode quantum efficiency larger than 20% is considered. The main requirements of the PMT are listed in table 3.1:

Table 3.1: Table of the main characteristics of ANTARES PMTs.

photocathode area	$\geq 500\ cm^2$
quantum efficiency	$\geq 20\ \%$
collection efficiency	$\geq 80\ \%$
TTS	< 3 ns
gain reached with HV > 2000 V	$\geq 5 \cdot 10^7$

Eventually, a 10-inches photocathode diameter PMT (Hamamatsu R7081-20 model) was chosen, with a gain of about $5 \cdot 10^7$ at high-voltage (< 2000 V).

The PMT is enclosed in a borosilicate glass sphere, 41.7 cm large in inner diameter and 15 mm thick. The sphere is designed to withstand high pressures of about 260 atm during operation and 700 atm during qualification tests. Its glass has a refractive index of 1.47 in the $300 \div 600$ nm range and the light transmission is larger than 95% above 350 nm, where most of Cherenkov photons are.

The influence of the Earth's magnetic field can degrade the transit time spread ($<$ 3 ns FWHM) of the PMT: thus a $\mu - metal$ grid with high magnetic permeability is installed between the PMT and the glass sphere using an optical gel. The optical gel was chosen with an appropriate refraction index to reduce the reflection. On the opposite side with respect to the PMT, an internal built-in LED is present. This is used for calibration purposes.

3.1.2   Storey

A storey is made of a triplet of OMs, a titanium container called Local Control Module (LCM) and additional instruments for the positioning and calibrations. The three OMs are equally spaced by 120° in the azimuthal angle and facing 45° downwards to increase the efficiency in the detection of upward-going particles. The LCM contains and protects the electronics from water, and is placed at the center of the storey. All the electronic boards are contained in the LCM, as well as the Slow Control (SC) instrumentation. The electronic boards control the distribution of the clock signal, the PMT HV supply and the readout of PMT signals.

The main electronic component is the Analogue Ring Sampler (ARS), which digitise, the signals coming from the OMs, providing information about its amplitude, arrival time and shape.
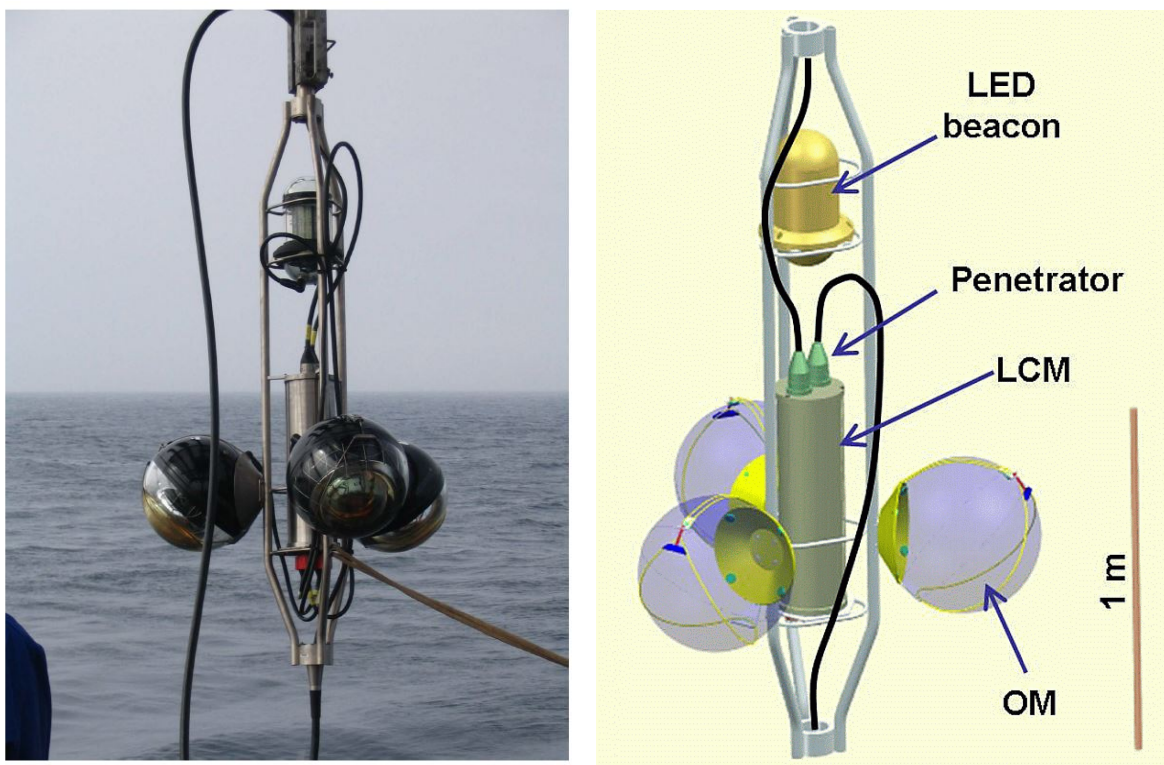
Figure 3.3: **Left**: Photo of a Storey before the deployment. **Right**: Schematic view of the Storey.

3.1.3   Line

A line is composed of 25 storeys equally spaced by 14.5 m and grouped in five sectors. It has a total length of ∼450 m. The lowest ∼100 m are not instrumented in order to avoid that, because of marine currents, material from the seabed could spread on the lowest OMs. The lines are anchored to the seabed by the Bottom String Socket (BSS) and held vertically using a buoy at the top of the line. The BSS contains the String Power Module (SPM), that controls the power supply to all the instrumentation of the line. In each sector, a Master Local Control Module (MLCM) contains the Ethernet switch to control data distribution from the storeys of the sector. Two of the lines have in their BSS also a Laser Beacon used for time calibration.

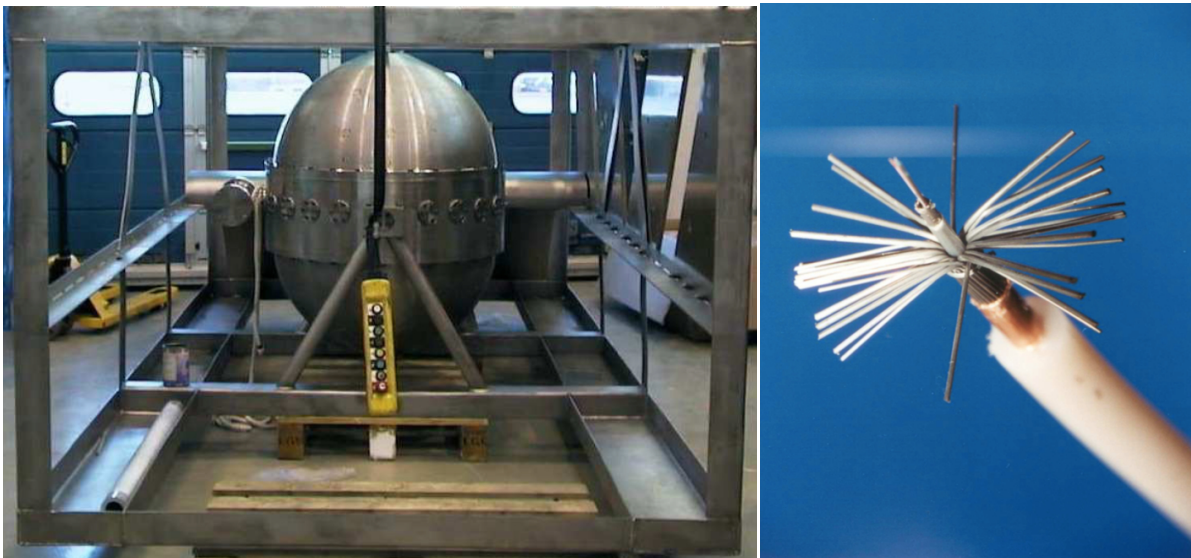### 3.1.4   The Junction Box and the electro-optical cable

Figure 3.4: **Left**: Picture of the Junction Box. **Right**: Picture of the electro-optical cable end.

The shore station and the detector are connected by the 42 km long Main Electro-Optical Cable (MEOC). It is made of 48 monomode pure silica optical fibres and has a diameter of 50 mm. By means of this cable the data acquisition control commands, the clock signal and the power supply is distributed to the whole detector and/or to its specific components and data transmission to shore is ensured.

The MEOC arrives from shore to the junction box, a titanium egg-shaped vessel. In the Junction Box (JB), the electrical and optical signals are split from the MEOC to the lines BSS. The JB is responsible for the distribution of power, clock signal and
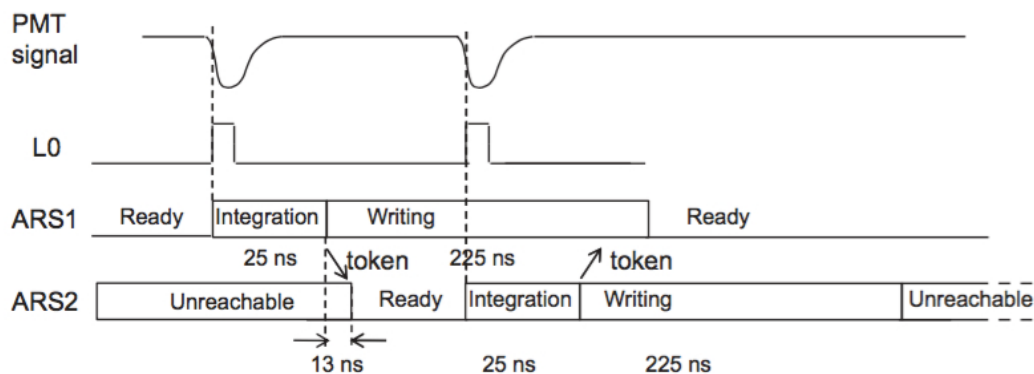
Figure 3.5: Working scheme of the ARS.

data transmission to the BSS and of bi-directional communication detween shore and the detector.

3.1.5 Data acquisition

The data acquisition system converts the analog signal from each PMT in a suitable format for the data analysis [56]. The main part of the system, the Front End Module, is located off shore, in the LCM, and is connected the two Analog Ring Samplers (ARS) coupled to each PMT [57]. The ARS is a customised chip, working in a token ring protocol for the digitisation of the analogue signals from the PMTs. The ARS has a charge threshold usually set at 0.3 photo-electrons to avoid spurious signals from dark currents, and integrate the PMT signal over a time window of about 30 ns. At the end of the integration window, the ARS enters a dead time of about 200 ns. After a token transmission time of about 13 ns, the second ARS starts looking for further signals over threshold and follows the same acquisition scheme. The time and charge information is digitised and constitute a *hit*.

Trigger

The ANTARES DAQ has different levels of triggers:

- "*Level zero*" (L0): hits with a charge larger than a low threshold typically set at 0.3 photo-electrons (p.e.) are selected;

- "*First level trigger*" (L1): hits within 20 ns on the same storey or with a large charge (with a tunable high threshold) are identified;

- "*Event trigger*" (L2): a trigger logic algorithm is applied to data and operates on L1 hits. L2 events are stored to disk.

The main physics triggers are the 3D-directional scan logic trigger *3N* and cluster logic trigger *2T3*. The 3N trigger processes all data and declares an event as soon as a minimum number of L1 hits are found within a $2.2\,\mu$s time interval. In addition, each pair of L1 hits should verify the causality relation:

$$\Delta t_{ij} \leq \frac{d_{ij}}{c/n} + 20ns \tag{3.1}$$

where Δt_{ij} and d_{ij} are the time difference and the spatial distance between $(\text{hit})_i$ and $(\text{hit})_j$ respectively, c is the speed of light and n the index of refraction of the sea water. The 2T3 trigger is based on the definition of a *T3 cluster* of hits. A T3 cluster is defined when two L1 hits among three adjacent storeys are in coincidence. The coincidence time window is set to 100 ns in case that the two storeys are adjacent, and to 200 ns in case of next to adjacent storeys. The 2T3 trigger logic requires at least two T3 clusters within a time window of $2.2\,\mu$s.

3.2 Water properties

The detector is located in deep sea water. As explained in chapter 1, water is one of the main actors of the detector since it is both the target for neutrino interaction and mean of light propagation. The knowledge of the optical properties of sea water at the ANTARES site is extremely important to understand the response of the detector and to produce and accurate Monte Carlo simulation (see §4.1).

3.2.1 Light transmission

The transmission of light in water is characterised by the processes of absorption and scattering of photons. Absorption reduces the number of photons that reach the PMTs. Scattering changes the direction of photon propagation and the distribution of their arrival time, and this worsens the event reconstruction performance.

The propagation of light in a transparent medium is quantified, for a given wavelength λ, by the medium optical properties coefficients. The absorption $a(\lambda)$, scattering $b(\lambda)$ and attenuation:

$$c(\lambda) = a(\lambda) + a(\lambda) \tag{3.2}$$

coefficients are defined so that, for each of them, a relative absorption, scattering and attenuation length is set. These lengths represent the path after which a beam of initial intensity I_0 and wavelength λ is reduced in intensity by a factor of $\frac{1}{e}$, according to the following relation:

$$L_i(\lambda) = i(\lambda)^{-1} \tag{3.3}$$

$$I_i(x,\lambda)) = I_0(\lambda)e^{-x/L_i(\lambda)}; \quad \text{i = a,b,c} \tag{3.4}$$
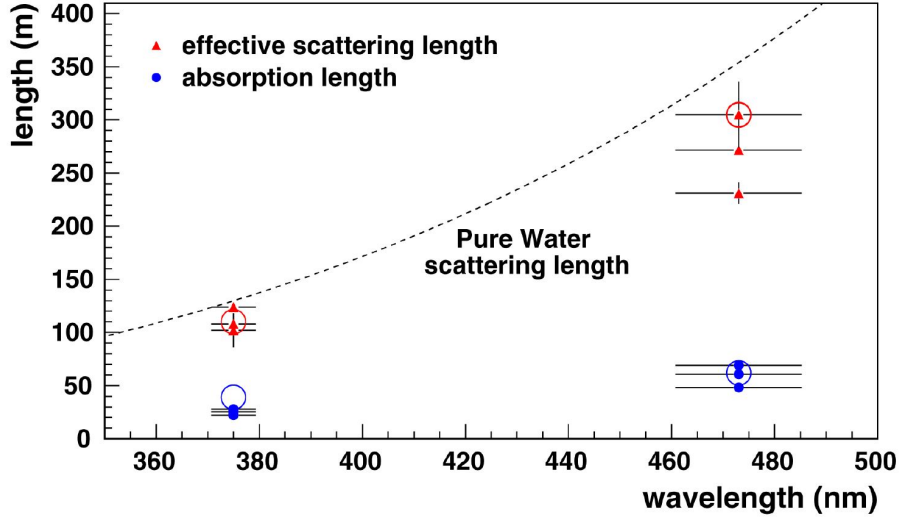
Figure 3.6: Water properties at the ANTARES site. The red and blue symbols represent the measured effective scattering and absorption length of light in water respectively at two different wavelength over different periods of time. The black dashed line shows, for comparison, the effective scattering length of light in pure water. Picture taken from [58].

where x is the optical path (in meters) traversed by photons.

The measured value of the effective attenuation length for a wavelength of 466 nm, in the ANTARES site [58], is:

$$L_c(\lambda = 466nm) = 41 \pm 1(stat) \pm 1(syst) \,[\text{m}] \tag{3.5}$$

3.2.2 Biofouling and sedimentation

The presence of particle sedimentation and bacteria which can stick on the OMs can reduce the light transmission through the glass sphere. These effects on the ANTARES optical modules have been studied in [59]. The experimental setup consisted of two glass spheres similar to those used for the OMs. One of them was equipped with five photo-detectors glued to the inner surface of the sphere at different inclinations zenith angles illuminated by two blue light LEDs contained in the second sphere. The loss of transparency, shown in figure 3.7, in the equatorial region of the OM is about 2% after one year, then shows some saturation effect. Considering that the PMTs of ANTARES are set at a zenith angle of 135°, biofouling and sedimentation should not represent a major problem for the experiment.

3.2.3 Bioluminescence and ^{40}K background

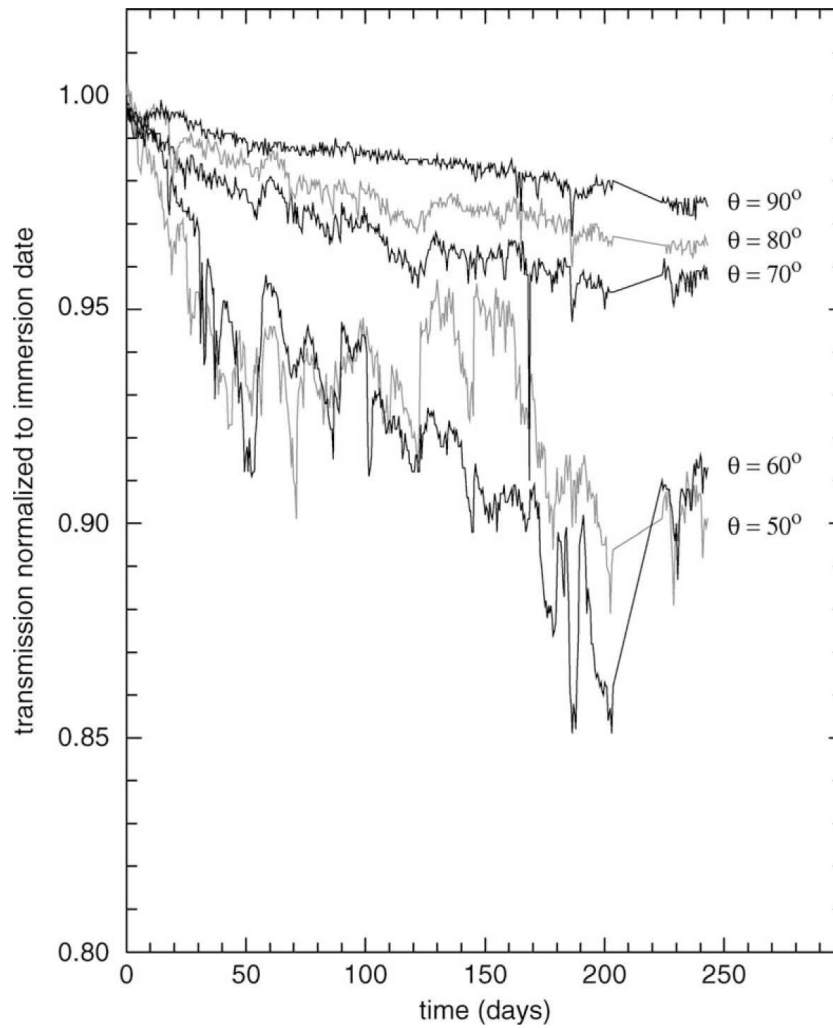Optical background in sea water is characterised by two components:

39

Figure 3.7: Light transmission as a function of time obtained from the immersion of the two glass spheres. Different curves correspond to different photodiode zenith angle. Picture taken from [59].
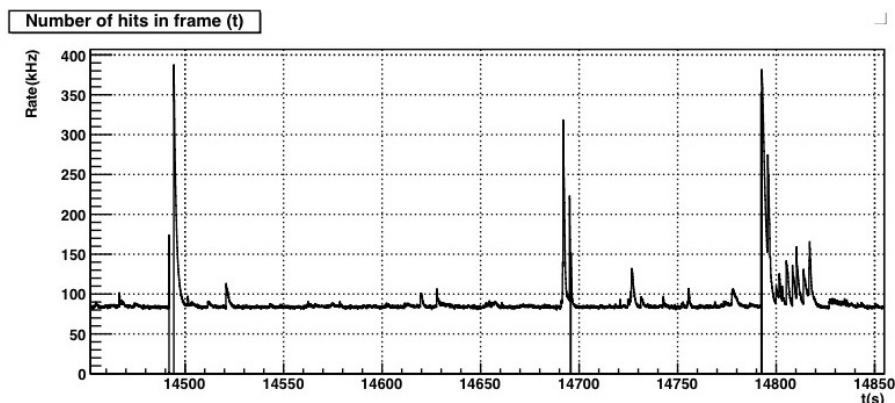
Figure 3.8: Median measured rate evolution on a OM.

- Decays of radioactive element;

- Bioluminescence.

The radioactive background is dominated by the ^{40}K decays:

$$^{40}K \rightarrow ^{40}Ca + e^- + \overline{\nu_e} \tag{3.6}$$

$$^{40}K + e^- \rightarrow ^{40}Ar + \nu_e + \gamma \tag{3.7}$$

In the first case, the produced electrons are often above the Cherenkov threshold. The $\gamma - ray$ of equation 3.7 has an energy of 1.46 MeV and can induce electrons above the Cherenkov threshold via Compton scattering. The intensity of this background is related to the salinity of the water, which is almost constant in all the Mediterranean Sea. The mean single rates from ^{40}K decays is around 50 kHz on a single PMT.

Besides the quite constant baseline due to ^{40}K decays the luminescence produced by living organism, the so-called bioluminescence, is also present. This background is found everywhere in oceans and there are two sources in deep sea: steady glowing bacteria and flashes produced by marine animals. The bioluminescence appears as bursts in the counting rates of PMTs, as shown in figure 3.8.

Seasonal effects in bioluminescence are also present and they reach their maximal intensity during spring: $\sim$ MHz single rates on PMTs can be detected. During these periods the detector may be switched-off to avoid damage to the electronics of PMTs.

Chapter 4

Analysis tools

In this chapter, the software tools developed by the ANTARES collaboration and used in the analysis are described. At first the Monte Carlo (MC) simulation chain is presented, then the reconstruction algorithms used in the analysis are discussed.

4.1   Monte Carlo simulations

Monte Carlo simulations are required in any high-energy physics experiment to understand the behaviour of the detector and its physics potential. The Monte Carlo chain developed for the ANTARES experiment can be considered as split into three main parts:

1. *Event generation*;

2. *Particles and light propagation*;

3. *Detector response simulation.*

Neutrino and atmospheric muon events are generated in the proximity of the detector, then they are propagated through the medium, Cherenkov light emission is simulated and photons are propagated to the OMs, including the PMTs response. Finally the optical background is added and the DAQ electronics and triggers are simulated.

Detector *"can"*

The instrumented volume is a cylinder containing all the PMTs. Around this volume there is a larger virtual cylinder, called the "can". It exceeds the instrumented volume by ~ 200 m which corresponds to about three light absorption lengths in the water. Outside this volume only the particle energy losses are considered for particle propagation. Inside the can the Cerenkov light is generated and propagated.
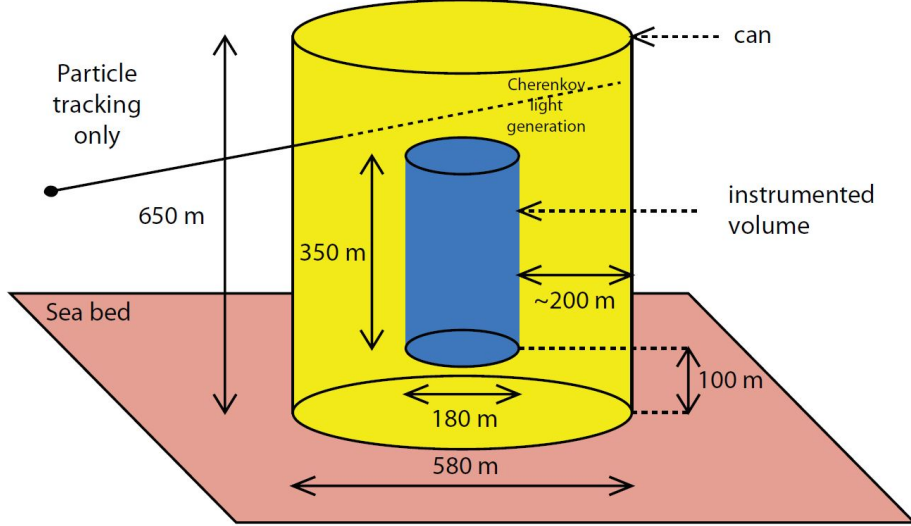
Figure 4.1: Definition of the ANTARES can. The can is built by extending the instrumented volume by three attenuation lengths (∼200 m), except from below where it is bounded by the sea bed from which no Cherenkov light can emerge.

4.1.1 Event generation

Neutrinos

Neutrino event generation is performed with the GENHEN package, based on the GEANT 3.21 software. A power law, $E^{-\gamma}$, is chosen for the generation spectrum of the neutrino interactions. This spectrum is weighted according to different neutrino fluxes to produce the event distribution for specific models. The simulation strategy foresees the definition of a volume around the detector which contains all potentially detectable neutrino interactions for the given energy range and simulate it within that volume. Any muon produced outside the can is propagated and stored if it reaches the surface of the can. The simulation volume for each event is defined by the maximum muon range (R_{max}) for a given neutrino energy in the generation bin. No neutrino interacting further away from the detector than this distance can produce a muon which will reach the detector. Hence this distance can be use to define the total simulation volume. The complete neutrino simulation follows these steps:

1. A cylindrical volume of radius R_{max} is defined around the instrumented volume of the detector.

2. A binned interacting neutrino spectrum (in $log_{10}(E_\nu/GeV)$ scale) is defined in the range between E_{min} and E_{max}. Then the number of events N, in each bin, is calculated.
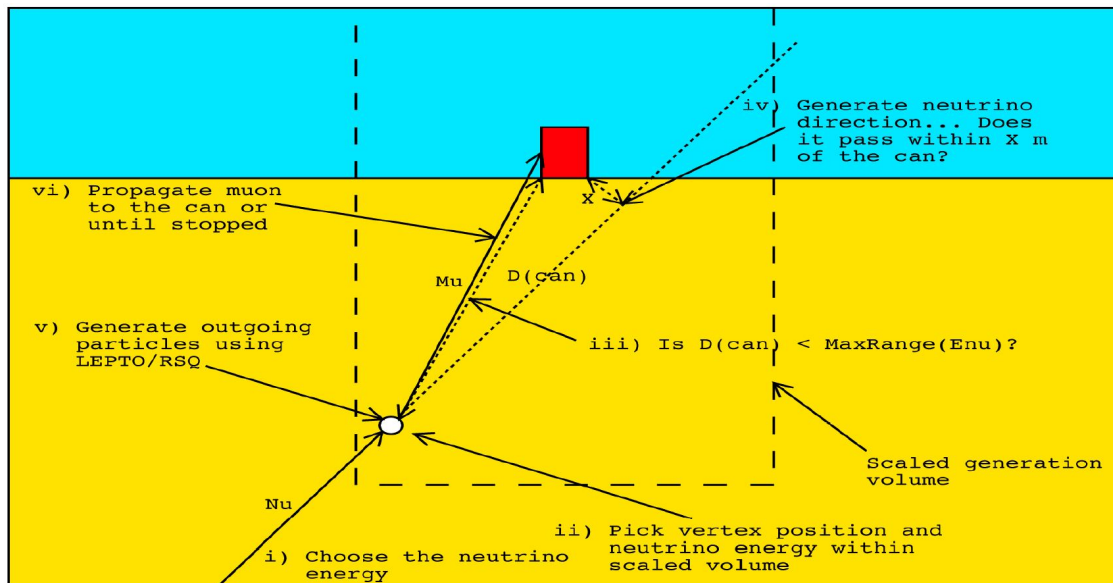
Figure 4.2: Schematic overview of the event generator algorithm GENHEN.

3. Using the maximum energy, in each bin, a maximum range in rock and water is calculated.

4. For each energy bin the numerical integration of the cross-section in LEPTO [60] is performed and the generation for this energy range is initialised.

5. Looping over the number of events N_{scaled}, for each bin:

   (a) The energy of the interacting neutrino is sampled from the $E^{-\gamma}$ spectrum within the energy range of the bin.

   (b) The neutrino vertex is chosen within the interaction volume.

   (c) Whether or not the vertex is inside the can is determined. If it is outside, the shortest distance from the neutrino vertex position to the can is calculated. If this distance is larger than the possible maximum muon range the event is discarded.

   (d) The neutrino direction is sampled according to an isotropic distribution. For events outside the can, it is calculated whether the distance of closest approach of the neutrino direction to the can is greater than some user specified distance. This avoids the generation of events that will not be detectable.

   (e) For each event, the neutrino interaction is simulated to get the final state particles at the neutrino interaction vertex.

44

(f) For events inside the can, all particles are recorded (position, direction, energy etc.) for further processing. For events outside the can, only muons are stored.

(g) At the end, the event weights are calculated and all events are written on disk.

Event weighting

By assigning a weight to each simulated event, it is possible to reproduce any spectrum defined according to a model, calculating the effective rates at the detector. Given a differential flux $\phi(E_\nu, \theta_\nu)$, the *global* weight is:

$$w_{global} = w_{gen} \cdot \phi(E_\nu, \theta_\nu) \tag{4.1}$$

where w_{gen} is the generation weight defined as:

$$w_{gen} = \frac{V_{gen} \cdot \rho N_A \cdot \sigma(E_\nu) \cdot P_{Earth}(E; \theta) \cdot I_\theta \cdot I_E \cdot E^\gamma \cdot F}{N_{total}} \tag{4.2}$$

- V_{gen} $[m^3]$: Generation volume;

- ρN_A: Product of the target density ρ for the Avogadro's number N_A that gives the number of target nucleons per unit volume;

- $\sigma(E_\nu)$ $[m^2]$: Total cross-section, as a function of the neutrino energy E_ν;

- $P_{Earth}(E_\nu; \theta_\nu)$: Probability for a neutrino to surviving crossing the Earth;

- I_θ $[sr] = 2\pi(cos\theta_{max} - cos\theta_{min})$: Angular phase factor depending on the considered range of $cos\theta_\nu$. It's the integral of the solid angle.

- I_E: Energy phase space factor depending on the input spectral index γ for the neutrino interaction rate. It's the integral of the energy spectrum between the minimum and maximum energy used in the generation.

- F: Number of seconds in one year.

- N_{total}: Total number of generated events.

Atmospheric muons

Cosmic rays interacting in the upper atmosphere produce extensive air showers that contain high energy muons. Although the ANTARES telescope is located at large depth under the sea, and exploits the shielding effect of water, the atmospheric muon flux at the detector is still very intense. An accurate simulation of this signal is mandatory to study the residual contamination of wrongly reconstructed tracks and to use the atmospheric muon tracks for calibrating the detector and testing the analysis software. Two possible approaches to the simulation of atmospheric muon bundles exist:

- *Complete simulation*: It is performed using dedicated software packages, as for example CORSIKA [61], that simulate extensive air showers starting from the first interaction of the primary particle and following the development of the shower through the atmosphere.

- *Parametric simulation*: This approach allows the production of an extremely large number of events within a reasonable CPU time consumption being based on the use on parametric formulas that describe the muon multiplicity, their distance from the shower axis and their energy spectrum within each bundle. The main drawback of this approach is the lack of flexibility in the choice of interaction and composition models.

In ANTARES, atmospheric muon bundles are generated using the MUPAGE software [62]. This is based on the parameterisation of the energy and multiplicity distribution of the muons inside a bundle. The parameterisation [63] has been built using a complete simulation, performed with the HEMAS software, and considering a composition model obtained by the MACRO experiment at the Gran Sasso laboratories [64]. MUPAGE allows the production of atmospheric muons in the range from 0° to 85° in zenith angle and covering the entire range of multiplicity and energy relevant for a neutrino telescope.

4.1.2   Particles and light propagation

All long-lived particles produced with the physics generators are tracked through the water in the can volume using a package called KM3 (a GEANT-based software developed in the ANTARES context). Every relevant physics process, like energy loss, multiple scattering, radiative processes and hadronic interactions is taken into account. The medium properties are fixed to the values at the experimental site. Muons propagation through the can volume is done by MUSIC [65]. The tracks are propagated in steps of 1 meter, taking into account all energy loss processes. Thanks to the homogeneity of sea water, a set of *scattering tables*, containing the probability of each photon to give a hit on a PMT as a function of 5 parameters is built. The parameters that are taken into account are:

- The distance of the OM from the muon.

- The photon arrival time.

- 3 angles defining the direction of the photons with respect to the muon and the PMT.

The probability for each Cherenkov photon to reach a PMT is extracted from these scattering tables. Similar scattering tables are created for electromagnetic showers. To have a reliable and fast simulation of the light produced in hadronic showers, the light
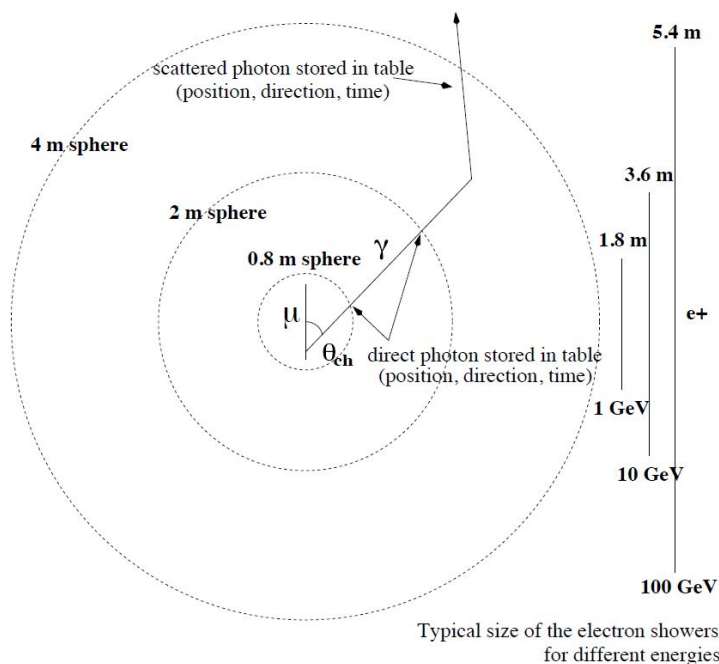
Figure 4.3: Schematic overview of the particles and light propagation.

production of each hadron is considered equivalent to that of an electron according to appropriate weight defined depending on the properties of each particle (*multi particle approximation*).

4.1.3 Detector response simulation and trigger

The detector response is simulated by the *TriggerEfficiency* program. This software, developed specifically for ANTARES, adds the hits due to the optical background to the hits coming from the event, then simulates the effect of the electronics and the trigger of events.

The first step adds to the MC events a fixed background rate specified by the user or taken from a real data run, according to a Poisson distribution. When real data are used in the run-by-run strategy, the program adds to the PMTs a background corresponding to what is measured in real data. This allows to consider not only the constant ^{40}K contribution, but also the optical background due to the biological activity that can vary depending on the season.

The electronics simulation reproduces the front-end board acquisition as described in §3.1.5. In order to simulate the time resolution, which is ~ 1.3 ns for single photo-electron signals and decreases for higher amplitudes, the hit times are smeared using a Gaussian

function with a width of $\frac{1.3ns}{\sqrt{N_\gamma}}$, where N_γ is the number of simultaneously detected photons. Analogously the hit amplitude is simulated by smearing the integrated number of photons with an empirical function that produces a (roughly Gaussian) smearing. The defined hits are then processed by a trigger simulator which reproduces what was presented in §3.1.5.

4.1.4 Run-by-run strategy

The Monte Carlo simulation strategy used for ANTARES is the so called *run-by-run* (rbr) [66]. For every physics run an analogous MC run is produced using the TriggerEfficiency option that take information from the data files and use it in the processing of the physics output of the Monte Carlo chain. This approach is used to take into account the variability of the conditions in a marine environment and their effect on the data acquisition. In particular the biological and physical phenomena that affect the measured rates show an evolving trend both in seasonal (long term) and daily (short term) time scale. Also, a temporary or permanent malfunctioning of a PMT is considered in this way. Finally, different triggers acting during a specific data acquisition run are considered.

4.2 Reconstruction algorithms

Triggered events must be reconstructed to obtain the physics quantities that are relevant for the analysis. In particular shower events. Shower events can be used in diffuse flux analysis because of the better achieveble energy estimation, if compared to the track-like events. On the other hand, track events provide a better angular relsolution, which can also be used to determine the origin of the event whether it is a neutrino or an atmospheric muon. In the following, the shower and track reconstruction algorithms used in this thesis are presented.

4.2.1 Shower Reconstruction

The TANTRA algorithm (**T**ino's **ANT**ARES Shower **R**econstruction **A**lgorithm) [67] allows the reconstruction of shower-like events for the ANTARES neutrino telescope. This has been specifically developed for the point-source search in ANTARES [68] and this work is its first application to diffuse flux analysis.
The reconstruction is performed according to the following steps:

1. Position hit selection: the set of hits with the largest sum of associated charge, causally compatible with a common source of emission, is selected.

2. Position reconstruction: a 4-dimensional least linear square pre-fit for the shower space-time position and, afterwards, an M-estimator fit for the refinement of this fit are performed.

3. Shower hit selection: hits that are compatible with the fitted position within a defined time residual window are selected.

4. Shower direction reconstruction: a probability density funcion (PDF) table based Log-Likelihood minimisation determines the neutrino direction and energy.

Position Reconstruction

A hit selection is necessary to reject background hits. The selection criterion for each pair of hits s:

$$|\vec{r}_i - \vec{r}_j| \geq c_w \cdot |t_i - t_j| \tag{4.3}$$

being:

- $\vec{r}_i$: position of the OM that recorded hit i.

- t_i: time of the hit i.

- $c_w = 0.217288$ [m $\cdot$ s^{-1}]: speed of light in water for the average Cherenkov light wavelength

This condition selects space-time correlated hits. Starting from this sample of hits, the shower vertex is defined assuming that the following relation is satisfied:

$$(\vec{r}_i - \vec{r}_{shower})^2 = c_w^2 \cdot (t_i - t_{shower})^2 \tag{4.4}$$

where i runs from 1 to the number of selected hits ($N_{SelectedHits}$); $\vec{r}_{shower}$ and t_{shower} are the shower vertex position and time. Then the system of equation is linearised by taking the difference between every pair of equation i and j:

$$(\vec{x}_i - \vec{x}_j)\,\vec{x}_{shower} - c_w^2 \cdot (t_i - t_j)\,t_{shower} = \frac{1}{2}\left[|\vec{r}_i^2| - |\vec{r}_j^2| - c_w^2\left(t_i^2 - t_j^2\right)\right] \tag{4.5}$$

The resulting linear equation system can be written as:

$$\mathbf{A}\vec{v} = \vec{b} \tag{4.6}$$

where:

- $\mathbf{A} = \begin{bmatrix} (x_1 - x_2) & (y_1 - y_2) & (z_1 - z_2) & -c_w(t_1 - t_2) \\ \vdots & \vdots & \vdots & \vdots \\ (x_{N-1} - x_N) & (y_{N-1} - y_N) & (z_{N-1} - z_N) & -c_w(t_{N-1} - t_N) \end{bmatrix}$

- $\vec{v}$: the four-dimensional space-time fit for the vertex.

- $\vec{b} = \frac{1}{2} \cdot \begin{bmatrix} |\vec{r}_1^2| - |\vec{r}_2^2| - c_w^2(t_1^2 - t_2^2) \\ \vdots \\ |\vec{r}_{N-1}^2| - |\vec{r}_N^2| - c_w^2(t_{N-1}^2 - t_N^2) \end{bmatrix}$

This equation system is solved with the method of the least linear square fit.

After this step, an *M-estimator* is calculated by minimising the following equation using the previous t result as the starting point:

$$M_{Est} = \sum_{i=1}^{N_{SelectedHits}} \left(q_i \cdot \sqrt{1 + \frac{t_{res,i}^2}{2}} \right) \tag{4.7}$$

where:

- q_i: charge of *i-th* hit ;

- $t_{res,i} = t_i - t_{shower} - |\vec{r}_i - \vec{r}_{shower}|/c_w$: *time residual* of *i-th* hit.

Direction reconstruction and energy estimator

Following this first fitting procedure, a further hit selection is performed. Based on the time residuals of hits with respect to the fitted shower vertex all hits fulfilling the condition:

$$-200 \text{ [ns]} < t_{res} < 500 \text{ [ns]} \tag{4.8}$$

are selected. The direction and energy of the neutrino are simultaneously fitted with a minimization of the negative log-likelihood function:

$$-\mathcal{L} = \sum_{i=1}^{N_{SelectedHits}} log\{P_{q>0}(q_i|E_\nu, d_i, \phi_i, \alpha_i) + P_{bg}(q_i)\} + \sum_{i=1}^{N_{unhitPMTs}} log\{P_{q=0}(E_\nu, d_i, \phi_i)\} \tag{4.9}$$

with:

- $P_{q>0}$: probability for a hit PMT to measure the observed charge.

- q_i: the charge of *i-th* hit.

- E_ν: neutrino energy.

- $d_i = |\vec{r}_i - \vec{r}_{shower}|$: distance between the shower and PMT with the *i-th* hit.

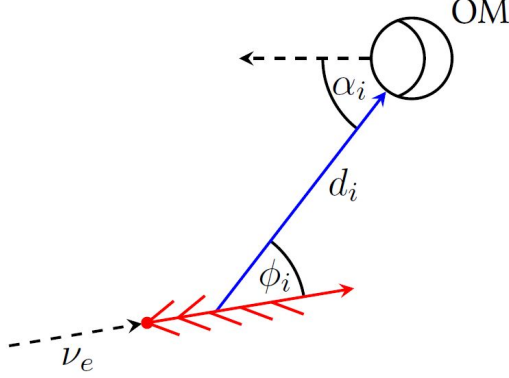- $\vec{r}_{shower}$: position of the shower.

Figure 4.4: Schematic overview of the geometric variables considered by the likelihood used in the direction reconstruction.

- ϕ_i: photon emission angle.

- α_i: photon impact angle on the OMT.

- P_{bg}: probability for a random background to have the measured charge.

- $P_{q=0}$: probability for a PMT of not being hit.

This likelihood depends on the shower vertex reconstruction; the PDFs are built using the MC simulation of showers in ANTARES. The signal term $P_{q>0}$ is the expectation value of the number of photons on a PMT, given the shower vertex-OM distance, the photon-emission angle and photon-impact angle. The number of emitted photons and therefore the number of photons expected on the PMT is proportional to the neutrino energy. The number of expected photons N is calculated for a 1 TeV shower from the MC and then scaled for different energy according to:

$$N(E_\nu) = N_{1 \text{ TeV}} \cdot \frac{E_\nu}{1 \text{ TeV}} \tag{4.10}$$

The overall probability to detect n photons, when the expectation is N, is given by the Poisson distribution:

$$P(n|N) = \frac{N^n}{n!} e^{-N} \tag{4.11}$$

In any case the OMs saturate at charges above about 20 p.e. preventing to determine the true number of arriving photons.

The non-hit term $P_{q=0}$ is the probability that a PMT does not have a hit. It is simply the Poisson probability to have zero charge when the expectation is N photons on the photocathode:

$$P(N) = P(q = 0|N) = e^{-N} \tag{4.12}$$

Finally the background term P_{bg} is the probability that an uncorrelated optical background event causes a hit with the observed charge. The distribution is taken from the ANTARES optical beacon runs, using all hits with hit times prior to the beacon flash.

Angular error estimator

After the best direction has been determined, the likelihood landscape around the fit is scanned along concentric circles of angular distances increasing in steps of 1 degree. When the likelihood value differs from the best fit by more than 1, this angular distance is used as the angular error estimate. This is not a rigorous estimate of the total angular error because, if the event has a very asymmetric likelihood landscape, the angular error estimator would only reflect the smallest component along the axes.

Algorithm performance

In plots 4.5 the algorithm performance, for events contained in a cylindrical volume of radius 300 m and high 250 m from the detector center, are shown. The shower position can be reconstructed with a precision in the order of 1 m. The angular resolution ranges between 3 and 10 degrees depending on the energy. The energy resolution of the order of about $5\% - 10\%$. These are the best performance for a shower reconstruction algorithm ever achieved in a neutrino telescope.

4.2.2   Track Reconstruction

In this thesis two track-event reconstruction algorithms, *AAFit* and *GridFit*, are used for the event selection. A brief description of the two and of the quantities specifically used in this work are reported in the following.

AAFit

The AAFit reconstruction algorithm [69] for track-like event is based on a likelihood fit composed by three consecutive steps, of increasing sophistication, that provide a starting point for the last likelihood fit. The likelihood function has several local maxima and the fit is successful only if the final minimisation procedure starts with track parameters that are already a good approximation of the optimal solution.

An hit selection analogous to that of TANTRA is applied, as well as a similar likelihood approach is used for the final fit. In this case, of course, time residuals are based on the hypothesis that hits are emitted by a muon track and the PDF is built accordingly. The following variable is used to characterise the quality of the fit:

$$\Lambda = \frac{log(L)}{N_{DOF}} + 0.1(N_{comp} - 1) \tag{4.13}$$
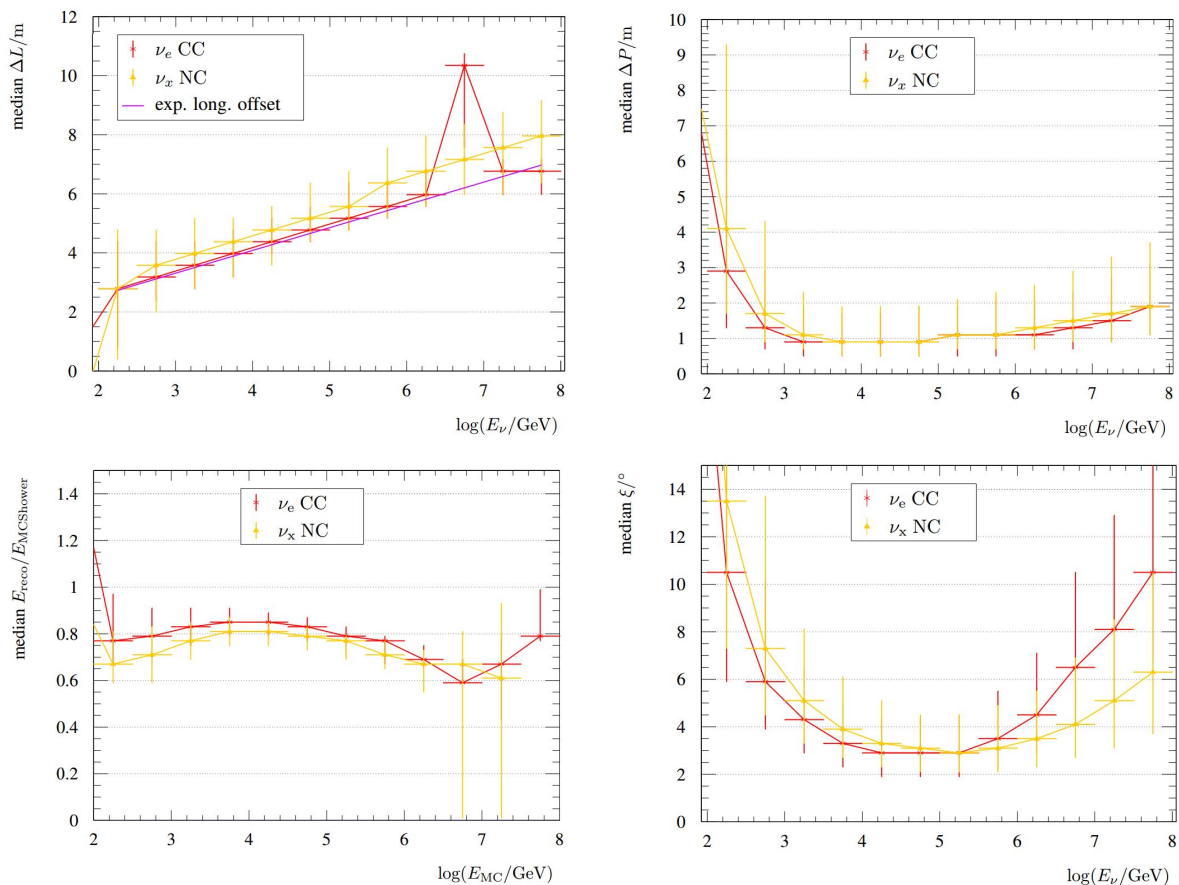
Figure 4.5: **Top-Left**: The distance between the position of the neutrino interaction vertex and the reconstructed shower position along the neutrino axis. **Top-Right**: The distance of the reconstructed shower position perpendicular to the neutrino axis. **Bottom-Left**: The ratio between reconstructed energy and the true Monte Carlo energy as a function of the shower energy. **Bottom-Right**: The angle between the directions of the reconstructed shower and the Monte Carlo neutrino as a function of the neutrino energy.

where:

- $\frac{log(L)}{N_{DOF}}$: log-likelihood per degree of freedom;

- N_{comp}: Number of compatible solutions found with the reconstruction algorithm.

GridFit

This algorithm works by binning the full solid angle in 500 different directions. For each one, the number of hits compatible with a muon track from this direction is determined and a likelihood fit is performed. The *GridFit Ratio* quality parameter is then computated as the sum of the compatible hits of all upward-going and all downward-going test directions:

$$R_{GF} = \frac{\sum_{up-going} N_{hits}}{\sum_{down-going} N_{hits}} \tag{4.14}$$

The lower this number, the higher the probability for of this event to be a downward-going muon.

Chapter 5

Diffuse flux analysis

In this chapter, the search method for very high-energy extraterrestrial neutrinos from unresolved sources using only shower like events is presented. The goal of this analysis is the identification, without any assumption on the source direction, of an excess of events produced by astrophysical sources over the expected atmospheric neutrino background.

5.1 Signal and Background definitions

As discussed in chapter 2, the IceCube signal and, in general, cosmic diffuse neutrino fluxes can be described with a power law with spectral indexes ranging from 2.0 to 2.7. A single-component unbroken power-law cosmic flux is used to describe the IceCube signal in this thesis. In order to have an estimation of the ANTARES sensitivities to different signal hypotheses, spectral index $\Gamma = 2.0$ or 2.5 will be considered in the following. The IC cosmic flux is then assumed to be isotropic, equally distributed among the three neutrino flavours and coming from the whole sky. In addition, symmetry between neutrinos and anti-neutrinos at their sources is considered. For this reason, from now on, using the word we will refer to the sum of ν and $\overline{\nu}$. The quantity $\Phi_{0,1f}^{-\Gamma}(E_\nu)$ describes the one-flavour neutrino flux normalisation at energy E_ν for an unbroken power-law neutrino flux with spectral index Γ. The considered test flux signal is:

$$\Phi_{0,1f}^{-2.0}(1 \text{ GeV}) = 1.0 \cdot 10^{-8} \text{ [GeV} \cdot \text{cm}^{-2} \cdot \text{sr}^{-1} \cdot \text{s}^{-1}] \tag{5.1}$$

$$\Phi_{0,1f}^{-2.5}(1 \text{ GeV}) = 6.0 \cdot 10^{-6} \text{ [GeV} \cdot \text{cm}^{-2} \cdot \text{sr}^{-1} \cdot \text{s}^{-1}] \tag{5.2}$$

For convention, the normalisation of this flux is also reported at 100 TeV:

$$\Phi_{0,1f}^{-2.0}(100 \text{ TeV}) = 1.0 \cdot 10^{-18} \text{ [GeV} \cdot \text{cm}^{-2} \cdot \text{sr}^{-1} \cdot \text{s}^{-1}] \tag{5.3}$$

$$\Phi_{0,1f}^{-2.5}(100 \text{ TeV}) = 2.2 \cdot 10^{-18} \text{ [GeV} \cdot \text{cm}^{-2} \cdot \text{sr}^{-1} \cdot \text{s}^{-1}] \tag{5.4}$$

For the normalisation at a different energy E, the fluxes must be multiplied by the factor $\left(\frac{E}{1\,\text{GeV}}\right)^{-\Gamma}$ and, to obtain the all-flavour normalisation, it must be multiplied by a factor three (under the assumption of a cosmic flux in flavour equipartition).

The background for this analysis is due to muons induced by upward-going atmospheric neutrinos and downward-going atmospheric muons that are wrongly reconstructed as upward-going. The neutrino background is described in the simulation with the conventional Honda flux [14], plus the prompt contribution due to the decay of short lived charmed hadrons as in the calculation of Enberg [18]. The conventional flux, coming from the decays of pions and kaons, is expected to be one power steeper than the primary CR spectrum at high energies; as a consequence the conventional component has spectral index Γ close to 3.7. The prompt component, coming from hadrons that are much shorter-lived, has the same spectral index of the CR at the top of the atmosphere ($\Gamma \sim 2.7$). Because of the different intensity of the conventional flux for muon and electron neutrinos (the prompt flux is equal for the two neutrino flavours), the cross-over between the two components occours at about hundred TeV region for ν_μ and at a few tens TeV for ν_e. The contribution from tau neutrinos in atmospheric fluxes can be neglected at the energy considered here.

5.2 Event selection

5.2.1 Run Selection

The data sample for this analysis starts from the 5-line period of ANTARES, in 2007, and covers the whole data acquisition of the telescope until the end of 2013, for a total livetime of 1405 days. The mean run durations is around 3 hours until 2013 when, in order to reduce the dead-time between two consecutive runs, it was increased to 12 hours. In figure 5.1 the duration of the acquisition time for each run considered in this analysis is shown.

The presence of bioluminescence and ^{40}K decays, described in chapter 3, introduces random background hits in the photomultiplier counting. The runs are classified according to a quality parameter (*Quality Basic* - QB) which depends on some parameters defining the environmental and acquisition condition. The QB value ranges from 0 to 4. The parameters used are:

- Baseline (BL): it is the average hit rate counting during the run for each PMTs;

- Burst-fraction (BF): the fraction of time, for each PMT, in which the rate is 20% above the mean value;

- SCAN-flag: this flag is assigned to runs whose acquisition setup is not standard.
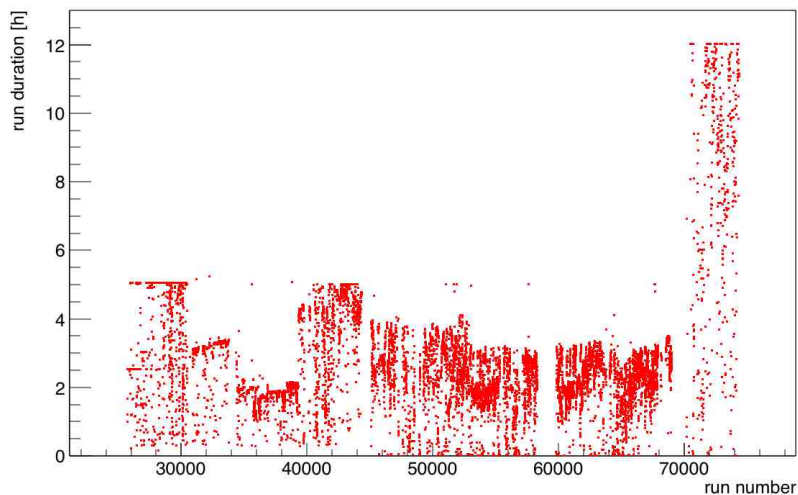
- Mean number of active OMs;

Figure 5.1: Run duration as a function of the run number for all the run sample used in this analysis.

- Mean number of active sectors;

- Mean number of active lines;

The QB value is:

- QB = 0: If the run duration is ≤ 1000 s, absolute timing errors or other problems are present. These runs are usually excluded from analyses.

- QB = 1: If are fulfilled basic selection, minimum requirement for a run to be included in the analysis:

  - run duration > 1000 [s];
  - at least one active ARS per OM;
  - no synchronization problems;
  - ($10\,\mathrm{mHz} \leq$ 3N trigger rate $\leq 10^5\,\mathrm{mHz}$);

- QB = 2: QB = 1 and at least 80% of the total number of OMs expected to work at the time of the run are effectively working:

- QB = 3: QB = 2 and BL $\leq$ 120 kHz AND BF $\leq$ 40%

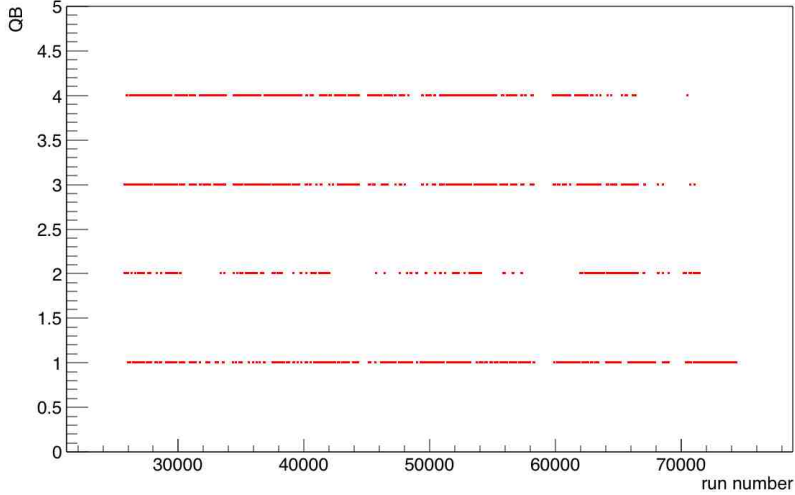- QB = 4: QB = 3 and BL $\leq$ 120 kHz AND BF $\leq$ 20%

Figure 5.2: Quality basic parameter as a function of the run number for all the run sample used in this analysis.

Figure 5.2 shows the Quality Basic for each run. In this analysis runs with $QB > 0$ have been used. A particular sample of runs, called *sparking-runs* and described in §5.2.3, are removed from the run selection to avoid any contamination in the signal region.

5.2.2 Event selection chain

The set of cuts applied for the selection of events was developed for a combined point-source analysis in which both track-like and shower-like events were used. One of the main aim of this work was to prove that this event selection is suitable also for a diffuse flux search. The selection chain is divided in three steps:

1. *Preselection cuts*;

2. *Intermediate cuts*;

3. *Model Rejection Factor (MRF) optimisation*.

All plots shown in this section and containing data follow the so-called *blinding policy* of the ANTARES collaboration. This rule limits the usage of data during the optimisation steps of the analyses to avoid any possible, even unintended, bias in the definition of the event selection procedure. At this level of the analysiss only runs with a run number that ends with the *0* digit are used. As a consequence, a livetime of 135 days is available for these checks. The results with the full data sample are discussed in §5.5.

5.2 Event selection

Preselection

During the the preselection step a set of simple conditions is applied:

1. *Trigger*: only T3 *or* 3N triggered events are selected.

2. *Muon-veto*: Events that are clearly track-like are excludede by selecting good reconstruction frmo AAFit:

$$\Lambda_{AAFit} > -5.2 \text{ and } \beta_{AAFit} < 1.0 \text{ and } cos(\theta_{zenith,AAFit}) > -0.1 \qquad (5.5)$$

3. *Containment*: Only events, whose reconstructed vertex is contained in a cylindrical volume around the detector center of radius ρ and height z, are considered.

$$\rho_{shower} < 300m \text{ and } |z_{shower}| < 250m \qquad (5.6)$$

4. *M-estimator*: A track-like event reconstructed by a shower-optimized algorithm, usually produces an event whose vertex is set far away from the detector. As a consequance, the $M_{estimator}$ takes large values since less hits can be correlated to the shower hypothesis. An addition cut:

$$M_{estimator} < 1000 \qquad (5.7)$$

is applied.

5. *Up-going*: A geometrical cut selects mostly upward-going showers:

$$cos(\theta_{zenith,shower}) > -0.1 \qquad (5.8)$$

6. *Angular error estimator*: An angular resolution better than 10 degrees is required:

$$\beta_{shower} < 10 \text{ [deg]} \qquad (5.9)$$

Intermediate cuts

Some further clever variables for the reduction of the muon background must be defined because of the reduced angular resolution of showers reconstruction, if compared to the track algorithms, and the possibility for muons to induce electromagnetic showers along their axis. These non-trivial selection criteria are the explained in the following.

1. *GridFit-Ratio*: Figure 5.3 shows the 2-D distribution of the GridFit Ratio and of the number of selected shower hits. It is evident that atmospheric muons follow a different behaviour with respect to signal events. The following geometrical condition considers only events external to an ellipse defined in the parameter space of GridFit and excludes from the sample atmospheric muons and neutrinos:

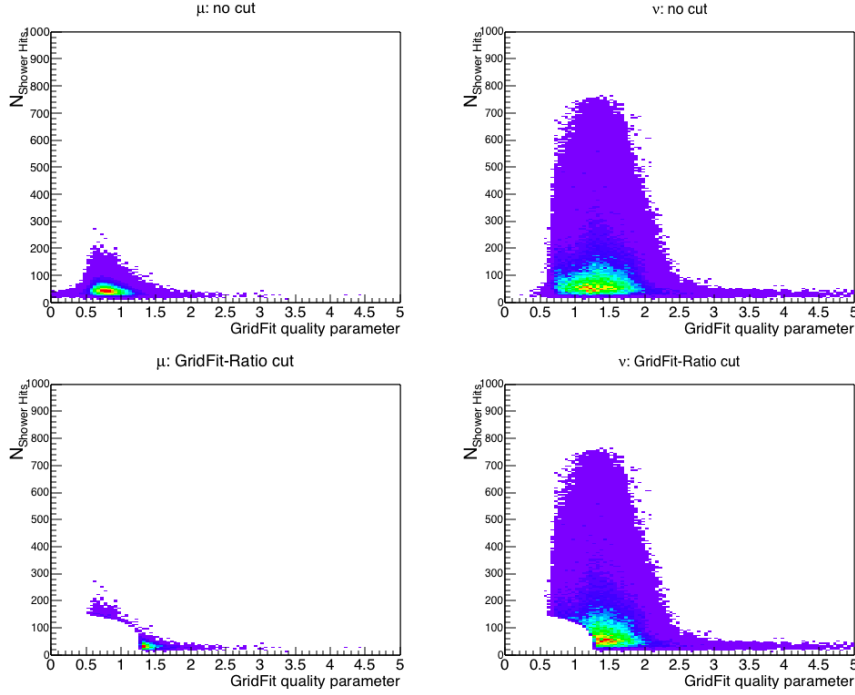$$\left(\frac{R_{GridFit}}{1.3}\right)^3 + \left(\frac{N_{ShowerHits}}{150}\right)^3 > 1 \qquad (5.10)$$

Figure 5.3: GridFit-Ratio cut on GridFit quality parameter and the number of selected shower hits space

2. *Likelihood-Ratio*: To discriminate between showers and atmospheric muons, a dedicated likelihood ratio variable has been defined. Track and shower likelihoods, considering only hits in coincidence on the same storey within 20 ns, are built from PDFs based on the following parameters:

   - time residual t_{res} of the hits;
   - number N of on-time hits $(-20 < t_{res}/ns < 60)$;
   - distance d of the hits from the reconstructed shower position.

   The likelihood is:

$$L = \sum_{hits} log(P_{sig}/P_{bkg}) + P_{sig} - P_{bkg} > 20 \qquad (5.11)$$

   with $P_{sig} = (N, d, t_{res}|shower)$ and $P_{bkg} = P(N, d, t_{res}|muon)$. The ratio between the shower and track likelihood provides a track/shower discrimination. Figure 5.4 shows its distribution.

3. *Charge-Ratio*: When the shower fit reconstructs a position along the muon track, one would expect photons induced by the muon arrive earlier than those predicted
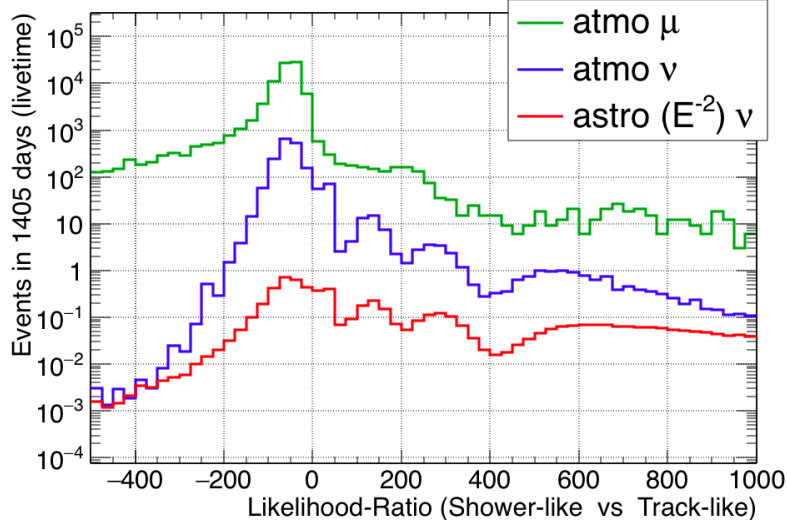
61

Figure 5.4: Likelihood-ratio parameter, after GridFit-Ratio and all previous cuts, to distinguish atmospheric neutrinos (blu) and muons (green) from showers due astrophysical neutrinos (red).

by a point source hypothesis. The charge ratio between the early and on-time hits was investigated and the distribution of the ratio of the two charge-sums is shown in figure 5.5. Considering the ratio of Q_{early}, the summed charge of all hits with a time residual:

$$-1000 \leq t_{res}/ns \leq -40 \tag{5.12}$$

and $Q_{on-time}$, the summed charge of all hits with time residuals of:

$$-30 \leq t_{res}/ns \leq 1000 \tag{5.13}$$

the ratio between these two charge values provides a further discrimination between tracks and showers as shown in figure 5.5. The chosen cut is:

$$ChargeRatio = \frac{Q_{early}}{Q_{on-time}} < 0.05 \tag{5.14}$$

Table 5.1 shows the effect of each cut in the selection chain. The rejection power for atmospheric muon is $\sim 10^5$, while retaining more then $1/3$ signal neutrinos. A strong reduction of atmospheric neutrinos is also achieved ($\sim 10^2$ rejection). This is mainly due to the fact that the atmospheric neutrino background is dominated by ν_μ events, most of which are track-like. The strength of these cascade searches is given by the possibility of topologically reject the largely abundant muon background.
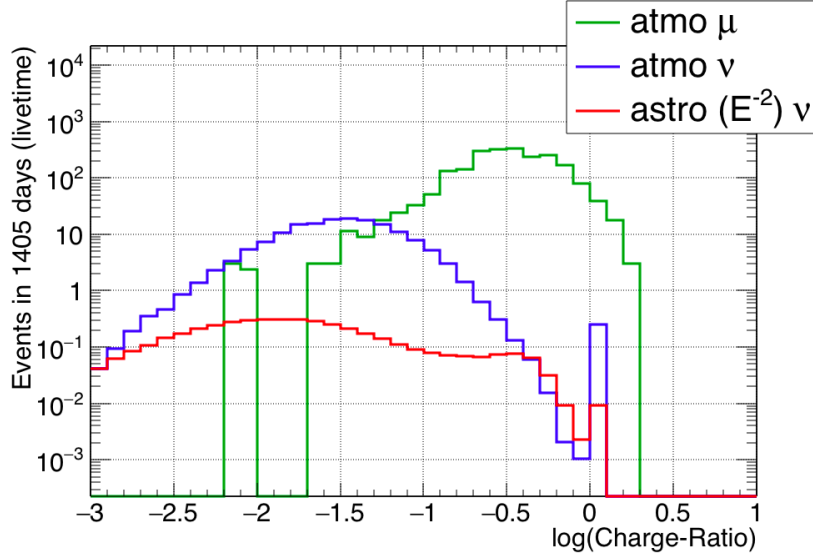
62

Figure 5.5: Charge-ratio parameter, after Likelihood-ratio and all previous cuts, to distinguish atmospheric neutrinos (blu) and muons (green) from showers caused by astrophysical neutrinos (red).

Table 5.1: Summary of the cut selection procedure. In each column the number of events after the cuts reported in the rows is shown for atmospheric muons, neutrinos and cosmic neutrinos. The ϵ values are the relative efficiency of each selection cut with respect to the preselection.

CUT	N - Atmo μ	N - Atmo ν	N - Astro ν	$\varepsilon_{atmo,\mu}$	$\varepsilon_{atmo,\nu}$	$\varepsilon_{astro,\nu}$
Preselection	$3.72 \cdot 10^6$	$2.07 \cdot 10^3$	9.89	1	1	1
GridFit-Ratio	$8.58 \cdot 10^4$	$1.67 \cdot 10^3$	7.34	0.02	0.81	0.74
Likelihood-Ratio	$2.18 \cdot 10^3$	146	4.44	$5.85 \cdot 10^{-4}$	$7.08 \cdot 10^{-4}$	0.45
Charge-Ratio	31.8	105	3.55	$8.55 \cdot 10^{-6}$	$5.1 \cdot 10^{-4}$	0.36

5.2.3 Sparking runs

The high voltage inside the PMTs sometimes creates a spark-over that becomes visible as a bright flash inside the OM. The device that should actually detect photons from showers, which are regarded as point-like light source, suddenly turns itself into a point-like light source. Such sparking events are not simulated in the RBR Monte-Carlo. This phenomenon has to be taken into account in shower analyses because sparking events mimick a high energy shower event.
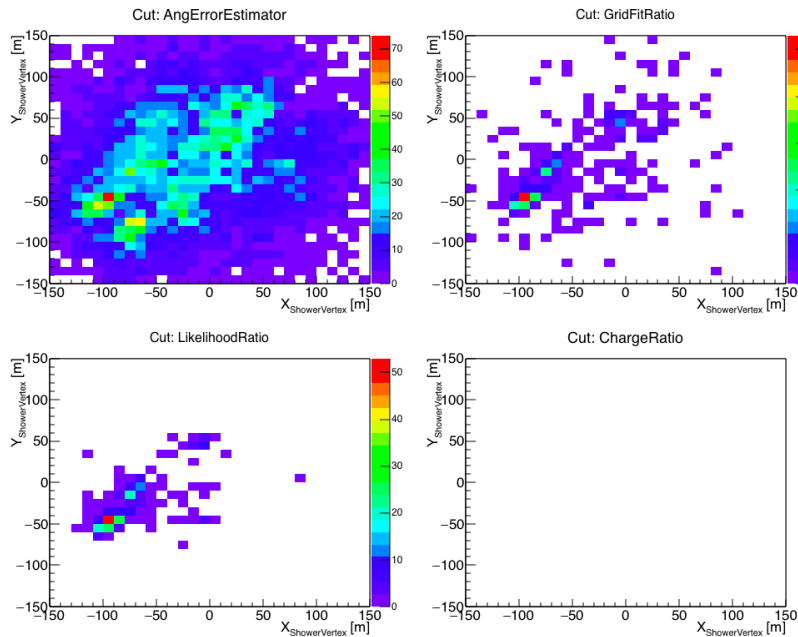
Figure 5.6: Cumulative distribution of the all known sparking runs. The plots represent the $x - y$ position of the reconstructed shower vertex respect to the detector geometrical center.

A small number of ANTARES runs, called *sparking-runs*, has been identified in past analyses with a high rate of sparking events. If a run is classified as *sparking* the complete run is excluded from the analysis. It has been checked the effect of the events selection chain on known sparking runs, in order to determine if a sparking event would eventually fall into the final sample of events. The danger is the concrete possibility that sparking events occur within a run that is not marked as *sparking*. In figure 5.6 the $x - y$ distribution of the reconstructed shower vertex is plotted, considering the cumulative distribution of all the 45 already known sparking runs for the period from 2007 to 2013. The distributions are shown at different levels of event selection. It is evident that the distributions show accumulation points on specific locations, corresponding to the sparking OMs. At the level of Charge Ratio cut, the final event selection cut, all the sparking events are rejected. We can then be confident that no sparking event from unknown passes the selection chain.

5.3 Data/MC comparison for *blinded* data sample

This section provides a collection of plots showing the comparison of the simulated Monte-Carlo events to real data. The comparison is given for the *blinded* 0-runs data,

while the MC is used with the complete livetime sample (1405 days) and scaled to the reduced data sample livetime (135 days). The variables for the comparison were chosen to highligh, in addition to the agreement of data and MC, the effects of the selection chain on the various components of the simulated flux. All the plots in fact report the various distribution after the cut on the Angular Error Estimator, the GridFit Ratio, the Likelihood Ratio and the Charge Ratio. All plots are shown with a cosmic neutrino spectral index $\Gamma = -2.0$ but all the following observations are also valid for the case with a spectral index $\Gamma = -2.5$.

In particular figure 5.7 shows the number hits used by the shower algorithm, figure 5.8 showes the reconstructed direction as function of the zenith angle, figure 5.9 shows the Likelihood Ratio distribution after the GridFit Ratio cut, figure 5.10 shows the Charge Ratio distribution after the Likelihood Ratio cut and figure 5.11 shows the reconstructed energy distribution after the Charge Ratio cut.

Where the dominant component is the atmospheric muon one data are a factor ~ 0.5 lower than the MC prediction. This can be due to the uncertainties on the atmospheric muon flux and the uncertainties on water properties. Concerning neutrinos, the data/MC agreement can be appreciated only after a substantial rejection of atmospheric muons. That is the case of last steps of the cut chain, like in the last two plots of figure 5.7 or 5.8. Here an agreement between data and MC closer to one is achieved. In conclusion, at the end of the selection, data and MC are in good agreement. Fluctuations can be ascribed to low statistics.

5.4   Model Rejection Factor optimisation

After the event selection, the events sample is mainly composed of atmospheric neutrinos, with a certain ($\sim 30\%$) contamination from surviving atmospheric muons. A cosmic neutrino event cannot be distinguished from an atmospheric one, as they are topologically the same. However cosmic neutrinos should follow a harder spectrum ($\Gamma \sim 2 - 2.5$) with respect to atmospheric neutrinos ($\Gamma \sim 3.7$ for conventional fluxes, 2.7 for prompt neutrinos). So, at a certain energy, the cosmic component overcome the atmospheric one and become visible. For ν_e fluxes this happens at about 30 TeV; the exact value depends on the assumed energy spectra.

The Model Rejection Factor (MRF) procedure [70] can be used to determine the optimal cut which provides the best upper limit given the expected number of background events and the expected behaviour of the signal. Let $\Phi(E)$ be the theoretical source flux, n_s the number of expected signal events, n_b the expected background and n_{obs} the number of events observed in a hypothetical experiment. If the number of observed events is compatible with the background, the upper limit for the flux al 90% confidence leve (C.L.)

(a) After: Angular Error Estimator

(b) After: GridFit-Ratio

(c) After: Likelihood-Ratio
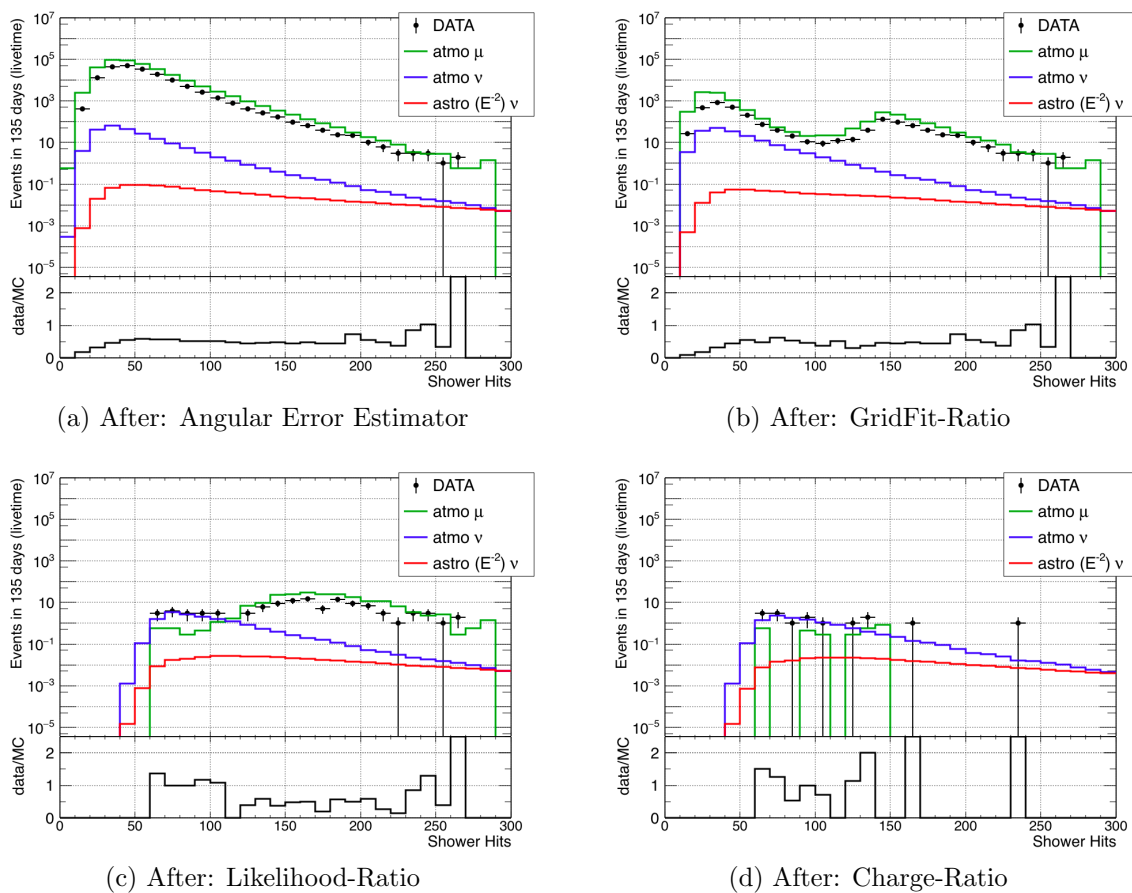
(d) After: Charge-Ratio

Figure 5.7: Data/MC comparison of the shower Number of Hits used in the shower reconstruction, where data are taken from the 0-runs. Starting from the plot ont the top-left side, all the preselection cuts are applied, then in order, are applied all subsequent cuts of the cut-chain that are the GridFit-Ratio, the Likelihood-Ratio and the Charge-Ratio.

(a) After: Angular Error Estimator

(b) After: GridFit-Ratio
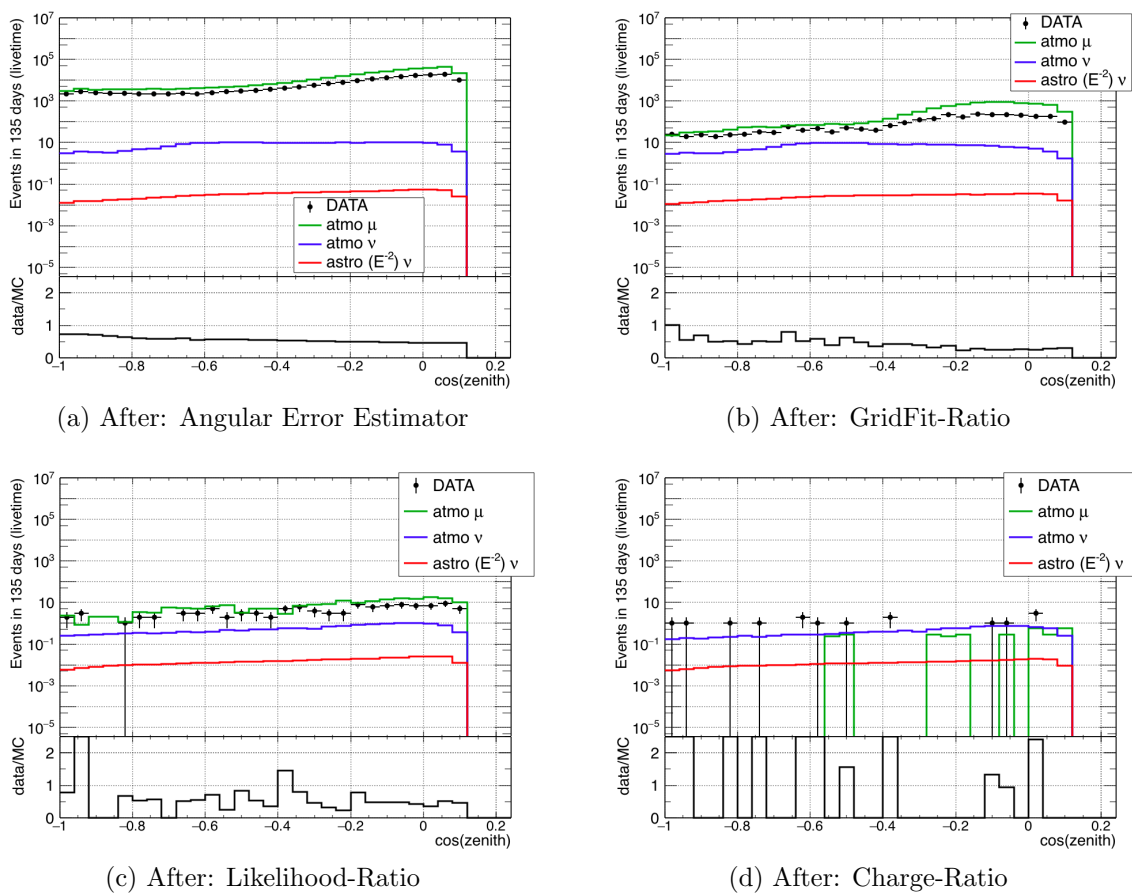
(c) After: Likelihood-Ratio

(d) After: Charge-Ratio

Figure 5.8: Data/MC comparison of the cosine of the reconstructed zenith of the shower, where data are taken from the 0-runs. Starting from the plot ont the top-left side, all the preselection cuts are applied, then in order, are applied all subsequent cuts of the cut-chain that are the GridFit-Ratio, the Likelihood-Ratio and the Charge-Ratio.
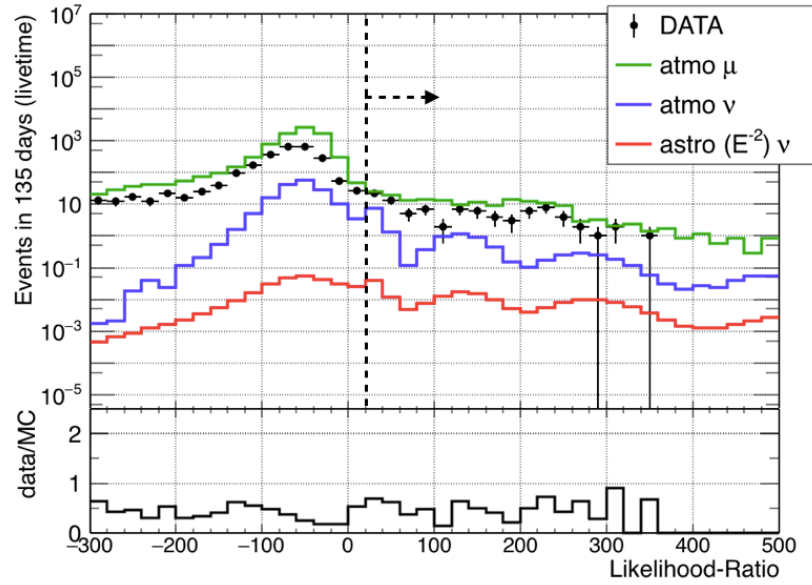
Figure 5.9: Data/MC comparison of the Likelihood-Ratio parameter, after GridFit-ratio and all previous cuts. The dotted line points where the Likelihood-Ratio cut acts.
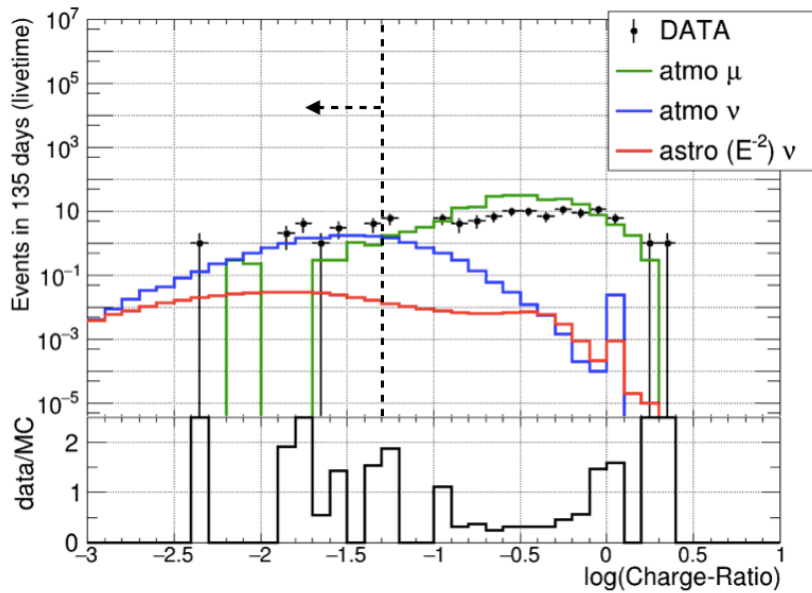

Figure 5.10: Data/MC comparison of the Charge-Ratio parameter, after Likelihood-ratio and all previous cuts. The dotted line points where the Charge-Ratio cut acts.
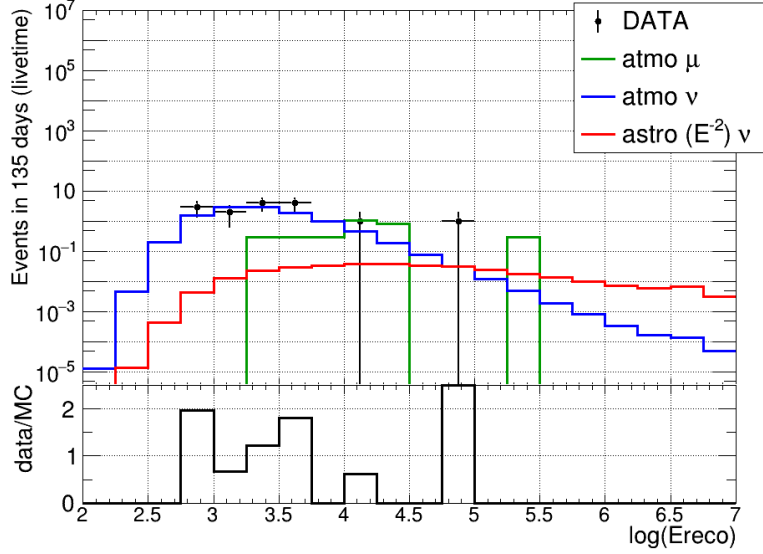
Figure 5.11: Data/MC comparison of the reconstructed shower Energy after all the cut-chain.

is:

$$\Phi(E)_{90\%} = \Phi(E) \cdot \frac{\mu_{90}(n_{obs}, n_b)}{n_s} \tag{5.15}$$

where $\mu_{90}(n_{obs}, n_b)$ is the Feldman-Cousins upper limit [71]. The *average upper limit* that would be observed by an ensemble of hypothetical experiments with no true signal ($n_s = 0$) and expected background n_b can be computed. Considering all the possible fluctuations for the estimated background, weighted according to their Poisson probability of occurrence, the average upper limit is:

$$\overline{\mu}_{90}(n_b) = \sum_{n_{obs}=0}^{\infty} \mu_{90}(n_{obs}, b_b) \cdot \frac{n_b^{n_{obs}}}{n_{obs}} \cdot e^{-n_b} \tag{5.16}$$

The best upper limit is obtained with the best cut that minimises the Model Rejection Factor (MRF):

$$MRF = \frac{\overline{\mu}_{90}}{n_s} \tag{5.17}$$

and hence minimises the average upper limit flux:

$$\overline{\Phi}(E)_{90\%} = \Phi(E) \cdot \frac{\overline{\mu}_{90}}{n_s} \tag{5.18}$$

or, equivalently, provides an estimate of the best sensitivity of the experiment.
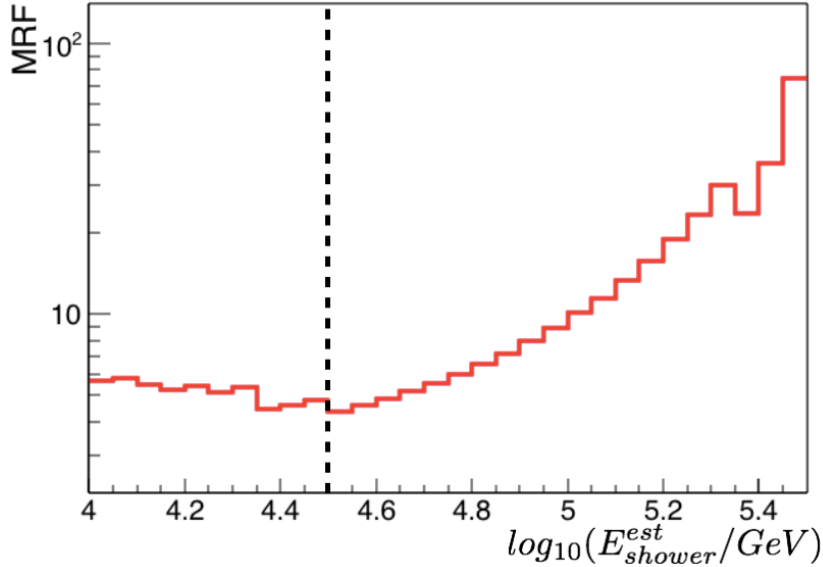
Figure 5.12: Model Rejector Factor for the $\Gamma = -2$ spectrum for a test MC sample.

The selection variable that is chosen to search for this optimal cut is the TANTRA energy estimator. The result of the procedure is the MRF value as a function of the cut energy as shown in figure [**?**]. Within the MRF optimisation it is found that cutting at:

$$E_{shower} > 30 \text{ TeV}, \tag{5.19}$$

after the whole chain of background rejecting cut previously described. The best upper limit at 90% confidence level (C.L.) are:

$$\Phi_{0,1f}^{90\%} = 3.1 \cdot \Phi_{0,1f}^{-2.0} \tag{5.20}$$

$$\Phi_{0,1f}^{90\%} = 2.3 \cdot \Phi_{0,1f}^{-2.5} \tag{5.21}$$

5.5   Results

The unblinding of the whole data sample has been granted by the collaboration. As a consequence all data from runs selected as described in §5.2.1 were made available for the analysis. The entire cut selection described in the previous sections has been applied. the As a result the unblinding of the full 1405 days sample gave 7 events surviving the selection chain and the energy cut at 30 TeV. The expectation from atmospheric backgrounds was of 5 ± 2 events, while 1.8 (1.3) signal events were expected assuming the signal flux of equation 5.2 (5.1). The uncertaninty on the background estimation comes

from the sum of uncertainties on the atmospheric neutrino flux and of the estimation of surviving atmospheric muons.

Figures 5.14 and 5.13 show the unblinded energy distribution for selected events. In the plots the expectations for a cosmic signal described by a power-law with spectral index $\Gamma = 2.5$ and $\Gamma = 2.0$ are depicted. The cut value is also shown and the slight excess of events with reconstructed energy larger than 30 TeV is visible.

Table 5.2 reports the event properties of the final sample after unblinding and applying the energy cut. In particular the run number in which the event occurred, reconstructed energy and zenith and the vertex position with respect to the centre of the detector are shown.

Finally, figure 5.15 shows the sensitivity of this analysis obtained from the MRF procedure. This is compared to the best fit for the cosmic flux observed by the IC collaboration and the predictions for atmospheric neutrino fluxes.

Table 5.2: Summary of the event properties for showers surviving the final selection cut including the energy selection.

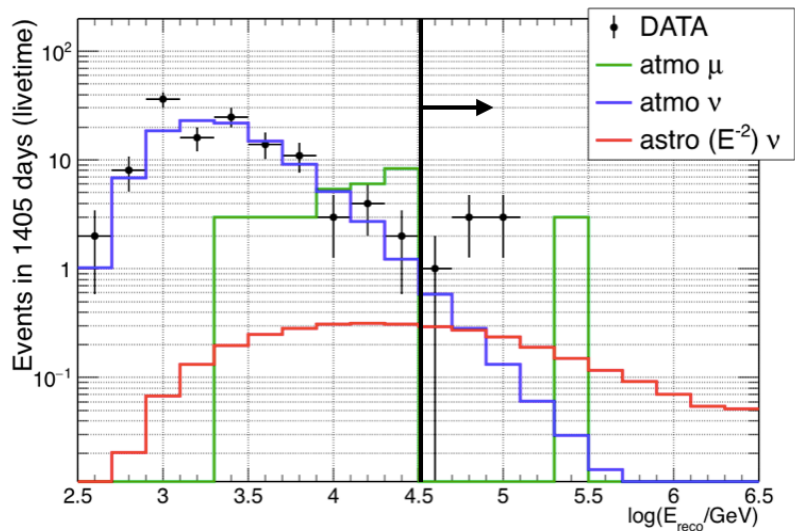| run number	E_{reco} [TeV]	θ_{zenith} [deg]	ρ_{shower} [m]	z_{shower} [m]
28722	55	110	45	3
38472	54	88	79	-102
38519	78	126	217	-27
39324	43	85	86	56
41839	104	105	163	150
54260	99	127	160	-164
71534	90	138	181	80

Figure 5.13: Unblinded reconstructed energy distribution for data and MC after the final selection cut. Colour code as in the legend. The cosmic neutrino flux is weighted for an E^{-2} energy spectrum. The energy cut at 30 TeV is shown as a solid black line.
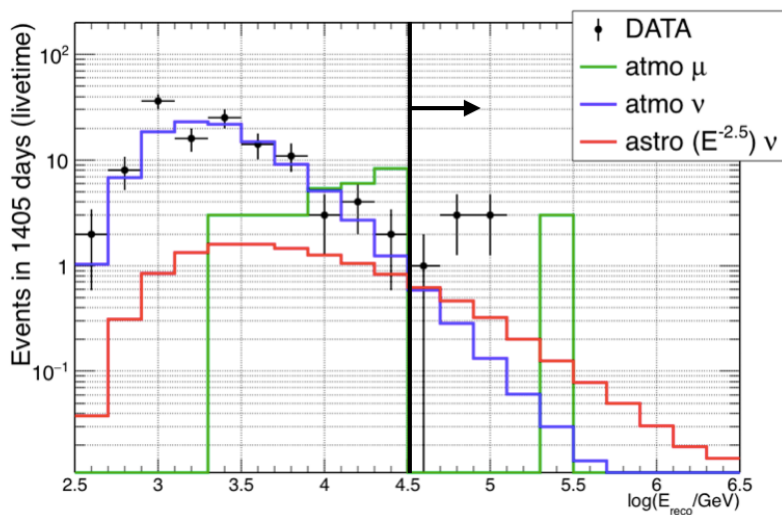

Figure 5.14: Unblinded reconstructed energy distribution for data and MC after the final selection cut. Colour code as in the legend. The cosmic neutrino flux is weighted for an $E^{-2.5}$ energy spectrum. The energy cut at 30 TeV is shown as a solid black line.
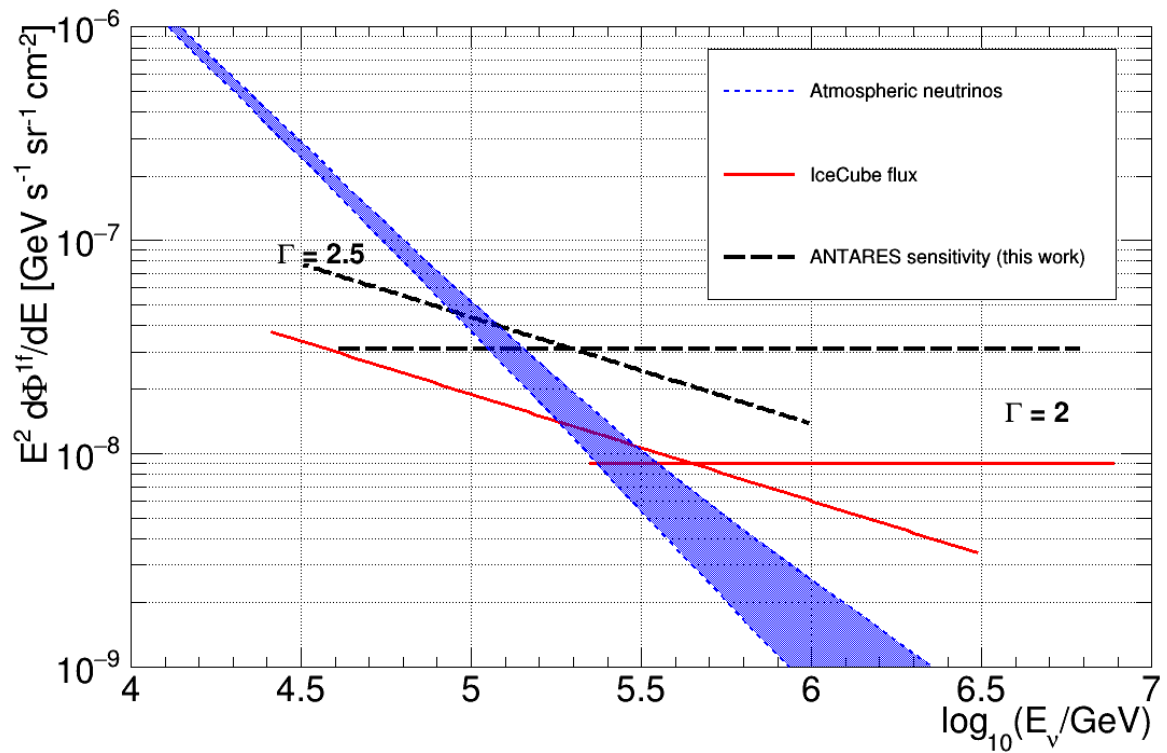
Figure 5.15: Comparison between the sensitivity obtained in this work (dashed black lines) with the expectations from atmospheric neutrino fluxes (blue shaded area) and the best fit for the IC signal with $\Gamma = 2$ and $\Gamma = 2.5$

Conclusions

The ANTARES telescope was completed in May 2008 and has taken data continuously since then, providing high quality neutrino data. The aim of the ANTARES Collaboration is to estabilish the existence of neutrino-emitting astrophysical objects, like AGN, GRB, and supernova remnants. The work presented in this thesis uses all data collected by the ANTARES neutrino telescope from the beginning of 2007 to the end of 2013.

The existence of cosmic high energy neutrinos has been estabilished with high significance by the IceCube Collaboration. The ANTARES detector is a complementary instrument of discovery with respect to the IceCube neutrino telescope, because of its different field of view and better event reconstruction capabilities.

The search for a diffuse signal of cosmic neutrinos analogous to that observed by IceCube is the subject of this thesis. In particular shower-like events allow a topological rejection of atmospheric muons. A series of event selecting variables is explained and used in this thesis. An enhancement of the signal over the background is expected at the highest energies because of the harder energy spectrum of cosmic events.

The optimal event selection is chosen using a Model Rejection Factor minimisation procedure to scan the possible energy cut. The resulting sensitivity is:

$$E^{-2.0}\frac{d\Phi}{dE} = 3.1 \times 10^{-8}[\text{ GeV}^{-1} \text{ s}^{-1} \text{ cm}^{-2} \text{ sr}^{-1}] \tag{5.22}$$

and

$$E^{-2.5}\frac{d\Phi}{dE} = 1.4 \times 10^{-5}[\text{ GeV}^{-1} \text{ s}^{-1} \text{ cm}^{-2} \text{ sr}^{-1}] \tag{5.23}$$

using the Feldman-Cousins upper limit estimation. The observation of data from the signal region provides an over-fluctuation with respect to the background estimation from Monte Carlo simulations. Indeed 7 events are observed over an expected background of 5±2.

Systematics uncertainties need to be evaluated in order to provide an upper limit estimation and/or an estimation of the significance of the event. The further extension of the data sample up to the end of 2016, together with the addition of events reconstructed in the track channel, can provide a further improvement of the sensitivity of the neutrino telescope, reaching a level that is expected to be close to what has been reported by the IceCube Collaboration.

Bibliography

[1] M.A. Markov, Proceedings Int. Conf. on High Energy Physics, p. 183, Univ. of Rochester, 1960.

[2] V.F. Hess, Phys. Zeit. **13**: 1084, 1912.

[3] A. M. Hillas, arXiv:astro-ph/0607109, 2006.

[4] E. Fermi, Phys. Rev. **75**: 1169, 1949.

[5] E. Fermi, Astrophys. J. **119**: 1, 1954.

[6] K. Greisen et al., Phys. Rev. Lett. **16**: 748, 1966.

[7] G.T. Zatsepin and V.A. Kuzmin, JETP Lett. **4**: 78, 1966.

[8] K. Hirata et al., Phys. Rev. Lett. **58**: 14901493, 1987.

[9] R. M. Bionta et al., Phys. Rev. Lett. **58**: 14941496, 1987.

[10] E. N. Alexeyev et al., Phys. Lett. B **205**(23): 209214, 1988.

[11] L. V. Volkova and G. T. Zatsepin, Soviet Journal of Nuclear Physics **37**: 212, 1980.

[12] T. K. Gaisser. Cosmic Rays and Particle Physics. Cambridge University Press, Cambridge, 1991. ISBN: 978-0521339315.

[13] G. D. Barr et al., Phys. Rev. D **70**: 023006, 2004. The extension of high energy is in 2009, available at http://www-pnp.physics.ox.ac.uk/barr/fluxfiles/.

[14] M. Honda et al., Phys. Rev. D **75**: 043006, 2007.

[15] G.D. Barr et al., Phys. Rev. D **74**: 094009, 2006.

[16] C.G.S. Costa, Astropart. Phys. **16**: 193, 2001.

[17] A. Martin et al., Acta Phys. Pol. B **34**: 3273, 2003.

Bibliography

[18] R. Enberg et al., Phys. Rev. D **78**: 043005, 2008.

[19] A. Abramowski et al., Nature **531**: 476, 2016

[20] S. Celli, A. Palladino and F. Vissani, arXiv:1604.08791, 2016.

[21] M. Su, T. R. Slatyer and D. P. Finkbeiner, Astrophys. J. **724**: 1044-1082, 2010.

[22] F. Vissani, arXiv:astro-ph/0609575, 2006.

[23] C. Distefano et al, Astrophys. J. **575**: 378-383, 2002.

[24] I. Di Palma, D. Guetta and E. Amato, arXiv: 1605.01205, 2016.

[25] K. Murase, arXiv:1511.01590, 2015.

[26] D. Guetta et al., Astropart.Phys. **20**: 429-455, 2004.

[27] M. Cirelli et al., JCAP **03**: 051, 2011.

[28] Raj Gandhi et al., Phys. Rev. D **58**: 093009, 1998.

[29] B. Pontecorvo, Zh. Eksp. Teor. Fiz. **34**: 247, 1958.

[30] J.D. Jackson, Classical Electrodinamics (3rd ed.), John Wiley, 1998. ISBN 978-0-30932-1.

[31] T. Chiarusi and M. Spurio, Eur. Phys. J. C **65**: 649-701, 2010.

[32] B. Hartmann. Reconstruction of neutrino-induced hadronic and electromagnetic showers with the ANTARES experiment. PhD thesis, University of Erlangen-Nurnberg, 2006. Available online at http://arxiv.org/abs/astro-ph/0606697.

[33] K.A. Olive et al. (Particle Data Group), Chin. Phys. C **38**: 090001, 2014.

[34] http://www.phys.hawaii.edu/dumand/

[35] I.A. Belolaptikov et al., Astrop. Phys. **7**(3): 263-282, 1997.

[36] V. Aynutdinov et al., Astrop. Phys. **25**: 140-150, 2006.

[37] A.V. Avrorin et al., Intruments and Experimental Techniques **54**(5): 649-659, 2011.

[38] T. Feder, Physics Today **55**(10): 20, 2002.

[39] http://antares.in2p3.fr/.

[40] S. Adrian-Martnez et al., Letter of Intent for KM3NeT 2.0, arXiv:1601.07459, 2016.

Bibliography

[41] F. Halzen, Eur. Phys. J. C **46**: 669-687, 2006.

[42] A. Karle et al., Proceedings of the 31st ICRC, Lodz, Poland, 2009.

[43] S. Adrian Martinez et al., Eur. Phys. J. C **73**: 2606, 2013.

[44] M. Spurio, Particle and Astrophysics. A Multi-Messenger Approach, Springer, 2014. ISBN 978-3-319-08050-5.

[45] P. Sreekumar et al., Astrophys. J. **494**: 523534, 2000.

[46] E. Waxman and J. Bahcall, Phys. Rev. D **59**: 023002, 1998.

[47] Wolfenstein L., Phys. Rev. D **20**(10): 26342635, 1979.

[48] S. P. Mikheev, A. Yu. Smirnov, Sov. Journ. of Nucl. Phys. **42**(6): 913917, 1985.

[49] M.G. Aartsen et al., Science **342**: 1242856, 2013.

[50] M.G. Aartsen et al., Phys. Rev. Lett. **113**: 101101, 2014.

[51] S. Adrian-Martnez et al., Phys. Lett. B **760**: 143148, 2016.

[52] M.G. Artsen et al., Phys. Rev. Lett. **114**: 171102, 2015.

[53] A. Loeb and E. Waxman, JCAP **05**: 003, 2006.

[54] A. Palladino and F. Vissani, arXiv:1601.06678, 2016.

[55] M. Ageron et al., Nucl. Inst. and Meth. in Phys. Res. A **656**(1): 1138, 2011.

[56] J.A. Aguilar et al., Nucl. Inst. and Meth. in Phys. Res. A **570**: 106, 2007.

[57] J.A. Aguilar et al., Nucl. Inst. and Meth. in Phys. Res. A **555**: 132, 2005.

[58] J.A. Aguilar et al., Astrop. Phys. **23**: 131-155, 2005.

[59] P. Amram et al., Astrop. Phys. **19**: 253-267, 2003.

[60] G. Ingelman et al., Comp. Phys. Comm. **101**:108 134, 1997.

[61] D. Heck et al., FZKA 6019, 1998.

[62] G. Carminati et al., Comp. Phys. Comm. **179**(12): 915-923, 2008.

[63] Y. Becherini et al, Astrop. Phys. **25**: 1-13, 2006.

[64] M. Ambrosio et al., Phys. Rev. D **56**: 1407, 1997.

Bibliography

[65] P. Antonioli et al., Astrop. Phys. **7**: 357, 1997.

[66] L.A. Fusco and A. Margiotta, Proceedings of the VLVnT 2015 Conference, Rome, 2015.

[67] T. Michael, PhD Thesis at the University of Amsterdam, 2016.

[68] T. Michael, Proceedings of the 34th ICRC, The Hague, Netherlands, 2015; arXiv:1510.04508.

[69] A. Heijboer et al., Proceedings of the 31st ICRC, Lodz, Poland, 2009; arXiv:0908.0816.

[70] G.C. Hill & K. Rawlins, Astrop. Phys. **19**: 393 (2003).

[71] G.J. Feldman and R.D. Cousins, Phys. Rev. D **57**: 3873-3889 (1998).